

<https://doi.org/10.1038/s41524-025-01594-6>

High entropy powering green energy: hydrogen, batteries, electronics, and catalysis

Check for updates

Guotao Qiu, Tianhao Li, Xiao Xu, Yuxiang Liu, Maya Niyogi, Katie Cariaga & Corey Oses

A reformation in energy is underway to replace fossil fuels with renewable sources, driven by the development of new, robust, and multi-functional materials. High-entropy materials (HEMs) have emerged as promising candidates for various green energy applications, having unusual chemistries that give rise to remarkable functionalities. This review examines recent innovations in HEMs, focusing on hydrogen generation/storage, fuel cells, batteries, semiconductors/electronics, and catalysis—where HEMs have demonstrated the ability to outperform state-of-the-art materials. We present new master plots that illustrate the superior performance of HEMs compared to conventional systems for hydrogen generation/storage and heat-to-electricity conversion. We highlight the role of computational methods, such as density functional theory and machine learning, in accelerating the discovery and optimization of HEMs. The review also presents current challenges and proposes future directions for the field. We emphasize the need for continued integration of modeling, data, and experiments to investigate and leverage the underlying mechanisms of the HEMs that are powering progress in sustainable energy.

The demand for clean and abundant energy sources grows every day, driven by climate change^{1–4}, rising energy consumption⁵, geopolitical tensions, and market volatility^{6,7}. Promising renewable sources such as solar, wind, hydropower, geothermal, and biomass face several implementation challenges, including low efficiencies, accessibility, and a lack of required infrastructures that render traditional fossil-fuel-based sources—coal, oil, and natural gas—techno-economically superior. Moreover, the efficacy of any of these approaches strongly depends on the location. For example, hydropower and geothermal have been highly effective for Iceland⁸ and Costa Rica⁹, two countries that generate their electricity almost entirely from renewable energy sources. In lieu of an energy “silver bullet”, new directions are being investigated. The ability to not only discover but also design new materials¹⁰ is essential for meeting the host of critical constraints of the energy industry¹¹, including enhanced functionality, robust stability, manufacturability, and having components that are abundant, replenishable, and safe.

High-entropy materials (HEMs)^{12,13} have emerged as a compelling solution for several energy challenges^{14–17}. HEMs are characterized by multi-element mixtures having multiple components occupying the same crystallographic sites in (near) equal measure^{13,18}. This random decoration of different elements boosts the material’s configurational entropy and enhances its thermodynamic stability¹⁹. Through entropy stabilization, new

—and sometimes counter-intuitive—chemistries have been realized²⁰, giving rise to a unique combination of properties, including exceptional thermo-mechanical properties, outstanding chemical stability, glass-like thermal conductivity, robust cyclability, and highly tunable catalytic binding energies¹³. The challenge lies in their discovery, as not all combinations of elements form single-phase, high-entropy systems.

Unlike conventional materials, where the properties can often be predicted and tested within a well-defined compositional space, HEMs span a vast and discontinuous compositional landscape due to the near-equimolar mixing of multiple elements^{19,21,22}. The number of possibilities renders exhaustive experimental exploration infeasible, creating an opportunity for computational and data-driven approaches. First-principles calculations and machine-learning models can rapidly screen through thousands of potential HEM compositions, predicting their structural stability, electronic properties, mechanical strength, and chemical reactivity before any experimental synthesis is attempted^{23–26}. Computational studies can also provide insights into the underlying mechanisms driving their performance—such as the effects of lattice distortions and different elemental combinations—and the influence of external conditions such as temperature, pressure, and radiation^{27–30}. These insights not only guide the rational design of new HEMs but also enable the optimization of existing systems for targeted applications.

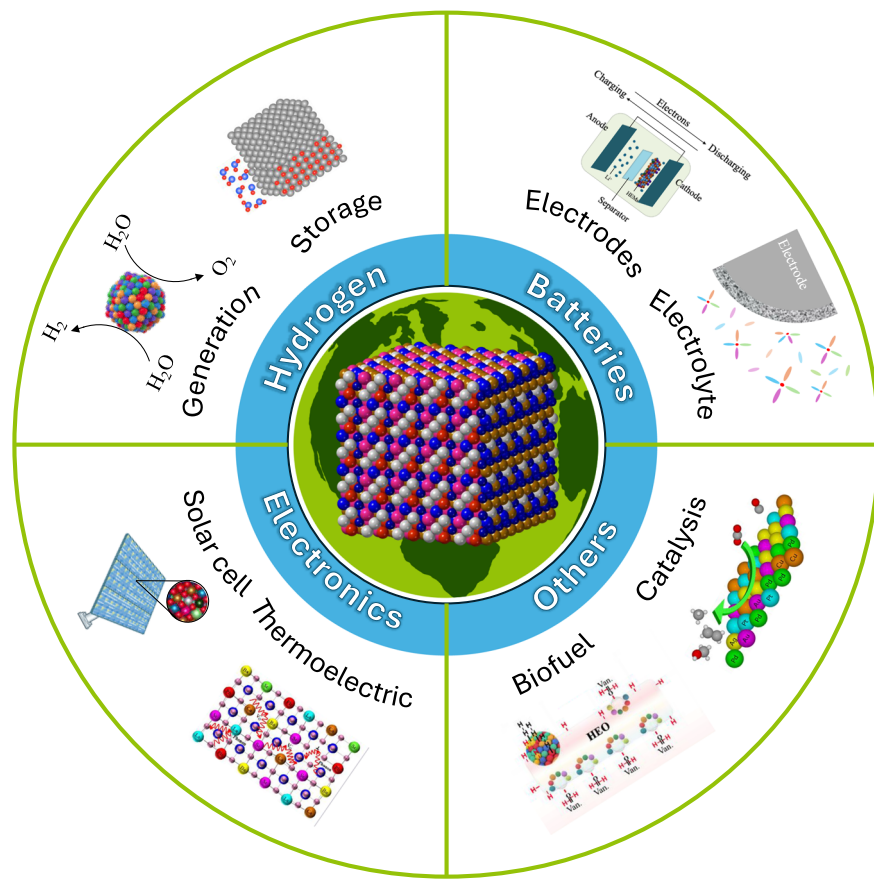


Fig. 1 | High-entropy materials for green energy applications. Reproduced with permission from American Chemical Society, Elsevier, and Wiley^{369–371}.

This review explores key green energy technologies that have been transformed by HEMs, including hydrogen generation/storage, fuel cells, batteries, electronics, catalysis, and biofuels (Fig. 1). The best performing chemistries and structures have been summarized and tabulated. The review highlights the crucial role of computational and data-driven methods to accelerate their discovery and optimization. Finally, current challenges are presented and future research directions are proposed, offering a comprehensive perspective on how HEMs can continue to drive innovation in sustainable energy.

High-entropy materials: definition and evolution

HEMs are a class of materials characterized by entropy contributions significant enough to play a role in their formation and stability¹³, which are governed by the minimization of the Gibbs free energy: $\Delta G = \Delta H - T\Delta S$, where H is the enthalpy (bonding and order), S is the entropy (randomness/disorder), and T is the temperature (disorder dial)^{18,27,31}. While there are several contributions to the entropy, including vibrational and electronic³², the dominant factor in HEMs tends to be configurational (S_{config})—arising in systems where multiple elements occupy the same crystallographic site. This scenario creates substitutional disorder in conventional alloys (e.g., steels, brasses, superalloys, and solders²¹), where an impurity (e.g., carbon in steel) replaces a fraction of the principal component (iron). If the replacement can be characterized as random/probabilistic—a scenario that becomes more probable with increasing temperature—then the arrangement of elements throughout the macroscopic crystal becomes non-unique. Disorder is a measure of the disparity in the accessible configurations^{10,18,27}. HEMs constitute the case where the random impurity concentration approaches that of the principal component—increasing the number of configurations and, accordingly, the entropy to a level of significant influence in ΔG . When designing these materials, it becomes convenient to define HEMs not by relative ΔH and

ΔS values, which can be cumbersome to quantify, but by the number of elements (at least 5) and their compositions (5–35 atomic %), a definition stemming back to the original HEM paper²². An interesting subset of HEMs is entropy-stabilized materials, where $T\Delta S$ causes ΔG to become negative—leading to formation/stability—indicating $\Delta H > 0$ ³³. These materials form from an entropy-driven solid-solid transformation having hallmark characteristics that can be measured experimentally¹⁹: (i) the transformation is reversible, temperature-driven, and goes from a multi-phase system (immiscible precursors) to a single phase, (ii) the transformation is endothermic—requiring heat, and (iii) the single phase constitutes a disordered system with the distribution of elements being random and homogeneous throughout the macroscopic crystal, i.e. no clustering or phase separation. For systems where the configurational entropy plays the dominant role, (iv) the transition temperature is minimized at equimolar concentrations where S_{config} is maximized. Importantly, entropy-stabilized materials need not have 5 components: there exist examples with only two elements on the same crystallographic site, including $(\text{Hf-Zr})\text{TiO}_4$ ^{33,34}. The first HEMs were discovered in 2004 and were composed exclusively of metallic components^{12,21,22} and have since been extended to new chemistries including oxides, borides, carbides, nitrides, chalcogenides, carbonitrides, and organic-inorganic hybrids^{13,35}.

Synthesis and prediction

HEMs can be synthesized via conventional solid-state reaction^{36–38}, high-temperature and high-pressure synthesis^{39–41}, spark plasma sintering^{42,43}, microwave-assisted methods^{44–46}, hydrothermal method^{47–49}, and solvothermal method^{48,50}. Table 1 details their advantages and disadvantages. Moreover, HEMs with different morphologies (e.g., fibers, thin films, nanoparticles, and nanosheets) can be processed by methods including physical vapor deposition^{51,52} and electrospinning^{53,54}.

Table 1 | Commonly employed synthesis methods for HEMs

Methodology	Description	Examples	Advantages	Disadvantages
Conventional solid-state-reaction	Mix solid precursors and heat them to a very high temperature for extended periods; atomic diffusion occurs, generating a thermodynamically stable product ^{344,345}	(FeCoNiCrMn) ₃ O ₄ ³⁶ , (MgCoNiZn) _{1-x} Li _x O ³⁷ , [(Bi,Na) _{1/5} (La,Li) _{1/5} (Ce,K) _{1/5} Ca _{1/5} Sr _{1/5}]TiO ₃ ³⁸	Simple process, flexible composition, solvent-free, low cost	High energy consumption, long reaction time (from hours to days), inhomogeneous reaction
High-temperature and high-pressure synthesis	Mix solid precursors and heat them to a high temperature under high pressure for extended periods	(FeCoNiCuRu)S ₂ ³⁹ , (La _{0.2} Nd _{0.2} Sm _{0.2} Eu _{0.2} Gd _{0.2}) ₂ Zr ₂ O ₇ ⁴⁰ , (Sr _{0.2} La _{0.2} Nd _{0.2} Sm _{0.2} Eu _{0.2})TiO _{3-δ} ⁴¹	Flexible composition, solvent-free, densified structure, high yield	High cost, high energy consumption, long reaction time (in hours)
Spark plasma sintering	A pulsed direct current is passed through the die and sample, achieving rapid heating of the sample to reaction ³⁴⁶	Ta _{1/6} Nb _{2/6} Hf _{1/6} Zr _{1/6} Ti _{1/6} , (La _{1/7} Nd _{1/7} Sm _{1/7} Eu _{1/7} Gd _{1/7} Dy _{1/7} Ho _{1/7} Zr ₂ O ₇) ₂ ⁴³	High purity, short reaction time (in minutes), densified structure	Expensive equipment required, possible inhomogeneous heating
Microwave-assisted methods	Polar molecules follow high frequency electric field from microwaves and release heat to drive the reaction ³⁴⁷ ; in electrical-conductive materials, charge carriers transport induced by the electric field heats the material ³⁴⁷	PtPdFeCoNi ⁴⁴ , IrFeCoNiCu ⁴⁵ , (Cr _{0.2} Fe _{0.2} Mn _{0.2} Co _{0.2} Ni _{0.2}) ₃ O ₄ ⁴⁶	Very short reaction time (in seconds), scalable process, energy efficiency, high purity	Temperature inhomogeneity in larger samples, porous structure
Hydrothermal & solvothermal methods	A reaction conducted in a closed system using a solvent under (near-)supercritical conditions ³⁴⁸	(CrMnFeNiZn) ₃ O ₄ ⁴⁸ , (FeCoNiCrCu) ₃ O ₄ ⁵⁰ , Pd@(YzrLaGdHf) _x O ₂ ³⁴⁹	Controlled particle size and morphology, low temperature requirement, homogeneous reaction, scalable process, eco-friendly (hydrothermal)	High cost, long reaction time, high energy consumption, impurity, safety concerns, solvent dependency, multi-steps

First-principles calculations such as density functional theory (DFT) can resolve the electronic structure of molecules and periodic systems, providing insights into the underlying mechanisms driving their formation, structure, and function. However, standard DFT cannot directly model chemically disordered systems. Instead, the community employs ordered approximants (supercells) to approximate these systems. Popular approaches include special quasirandom structures (SQS)⁵⁵ and the small cells construction as implemented in the *aflow++* partial occupation module^{18,27}. SQS mimics chemical disorder in the infinite-temperature limit by resolving supercells that minimize atomic-occupancy correlations, which in practice are often large and low-symmetry, and therefore computationally expensive. Instead, the small cells construction creates an ensemble of minimally sized supercell approximants of varying correlations that are easily parallelized on standard computing clusters. The approach captures the range of accessible configurations at a fixed cell size and can resolve finite-temperature effects approaching the order-disorder transition⁵⁶. Beyond pure quantum treatments, classical molecular dynamics (MD) with empirical and semi-empirical force fields allows for larger length- and time-scales but sacrifices some electronic detail. In contrast, quantum MD retains electronic fidelity but is constrained by system size and sampling efficiency⁵⁷. Machine-learning (ML) force fields bridge this gap by training on DFT data to achieve near-DFT accuracy for systems with tens of thousands of atoms, thereby capturing local disorder and defect dynamics^{58,59}. In a study of high-entropy carbides, ML models trained on thermodynamic data accurately predicted entropy-forming-abilities—a computational descriptor describing the likelihood that a composition forms a single-phase HEM based on the small-cells construction²⁰—aligning well with DFT results. Moreover, ML analyses reveal that high entropy-forming-ability correlates with minimal short-range chemical order, emphasizing the role of disorder in stabilizing HEMs²⁶. Monte Carlo simulations facilitate rapid compositional and configurational screening, identifying stable phases, solute distributions, and preferential site occupancies^{60–63}. CALPHAD-based phase diagram calculations, have proven instrumental in identifying promising alloy compositions with tailored phase fractions and mechanical properties, thus streamlining subsequent experimental verification⁶⁴. As high-throughput databases and computational resources continue to expand, coupling DFT with ML- and artificial intelligence (AI)-based algorithms enables the rapid screening of thousands of potential HEM compositions, predicting their structural stability, elastic properties, and catalytic performance in a fraction of the time required by experiments and trial-and-error calculations^{23–26}.

Large-scale, general-purpose repositories such as *aflow.org*⁶⁵, Materials Project⁶⁶, and OQMD⁶⁷ support these efforts by providing extensive electronic-structure data across a broad range of compounds. Meanwhile, HEM-focused databases like the Consolidated Database of High Entropy Materials⁶⁸ collect experimentally-measured mechanical properties. The TCHEA7 thermodynamic/properties library, part of the CALPHAD ecosystem⁶⁹, provides detailed thermodynamic and property data specific to HEMs.

Hydrogen

Hydrogen generation

Hydrogen is abundant in compound form (e.g., hydrocarbons, water) and is generated by reacting these compounds to release H₂. The typical approach is steam reforming, which reacts hydrocarbons with water and generates significant greenhouse gases in the process. Instead, H₂ can be produced from water with zero emissions using renewable-powered electrolysis, i.e. using electricity generated from sources such as solar⁷⁰, wind⁷¹, and hydro⁷². Electrolysis splits water into hydrogen and oxygen, involving two half-reactions occurring at the cathode and anode electrodes of an electrochemical cell: the hydrogen evolution reaction (HER) and the oxygen evolution reaction (OER), respectively. HER generates hydrogen gas (H₂) by reducing water, whereas OER generates oxygen gas (O₂) by oxidizing water.

In recent years, HEMs have emerged as promising catalysts for hydrogen generation, benefiting from a “cocktail effect” of different elemental components that enhances activity/stability and cannot be attributed to any single component. By altering composition or stoichiometry, local electronic environments and oxidation states can shift significantly, rendering it possible to tailor catalytic behavior for optimal performance²³. For example, nanosheets of Co_{0.6}(VMnNiZn)_{0.4}PS₃ (2022), which adopt a monoclinic crystal structure (space group C2/m), demonstrate exceptional HER performance with an overpotential of 65.9 mV at a current density of 10 mA cm⁻² and a Tafel slope of 65.5 mV dec⁻¹⁷⁴. The high-entropy sheet geometry, offering higher concentrations of sulfur and manganese sites on the edges and phosphorus sites on the basal plane, contributes significantly to its HER performance (Fig. 2a, b). The single-phase face-centered cubic (fcc) Ni₂₀Fe₂₀Mo₁₀Co₃₅Cr₁₅ (2018) exhibits high corrosion resistance and stability in both acidic and basic electrolytes—having an overpotential of 107 mV in acidic solutions and 172 mV in basic solutions at a current density of 100 mA cm⁻² (Fig. 2c)—outperforming many traditional catalysts

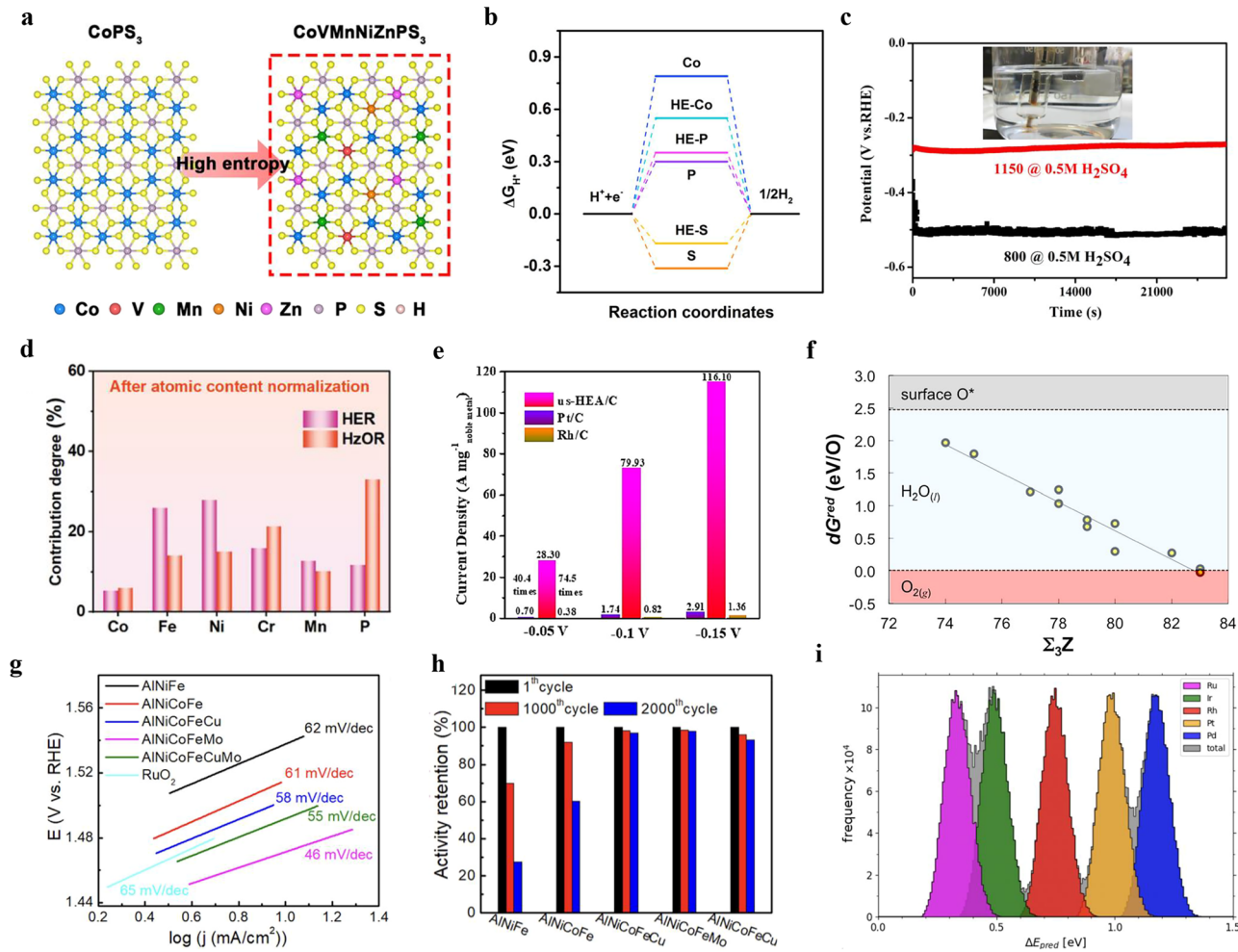


Fig. 2 | Water electrolysis and fuel-cell reactions. **a** Illustrations of CoPS_3 and high-entropy counterpart CoVMnNiZnPS_3 ⁷⁴. **b** Free-energy diagram of the edge sites in CoPS_3 and CoVMnNiZnPS_3 for the hydrogen evolution reaction (HER)⁷⁴. **c** Electrochemical stability of the $\text{Ni}_{20}\text{Fe}_{20}\text{Mo}_{10}\text{Co}_{35}\text{Cr}_{15}$ performing HER in 0.5 M H_2SO_4 after annealing at 1150 °C and 800 °C for 1 h⁷⁵. **d** The degree to which each metal in CoFeNiCrMnP contributes to the HER and hydrazine oxidation reaction (HzOR)⁷⁷. **e** Comparisons of the mass activities of ultrasmall high-entropy alloy NiCoFePtRh supported on carbon (us-HEA/C), commercial Pt/C, and commercial Rh/C at different potentials⁶. **f** Differential reduction free energy (dG^{red}) of adsorbed atomic oxygen on a randomly chosen subset of sites on the CoCrFeNi

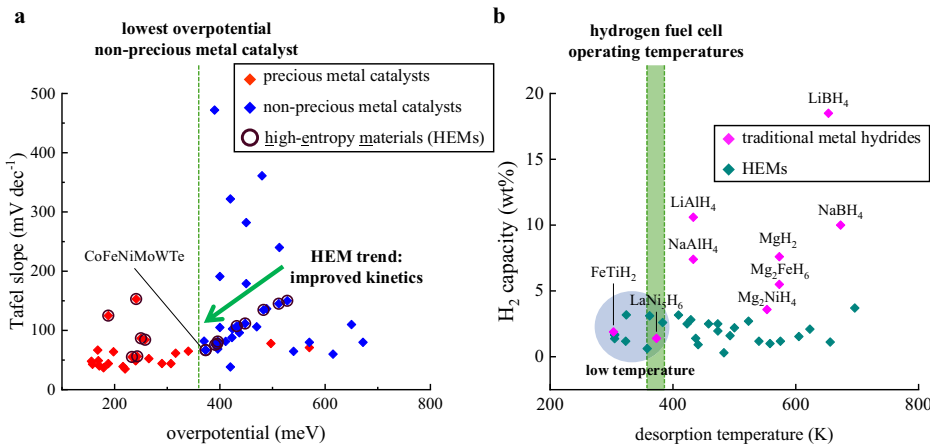
HEM surface vs. the sum of the atomic numbers of the three metal atoms defining the site ($\Sigma_3 Z$)⁷⁹. Shaded regions illustrate different stable phases of O: adsorbed O atom (>2.47 eV), liquid water (referenced to gas-phase O_2 and H_2 at the standard state; <2.47 eV), and gas-phase O_2 (<0 eV). **g**, **h** Tafel curves and current retentions of nanoporous HEMs and ordered counterparts while performing oxygen evolution reaction⁸⁴. **i** Near-continuous ${}^*\text{OH}$ adsorption energy spectra during the oxygen reduction reaction on IrPdPtRhRu⁸⁷. **(a, b)** and **(e–h)** are reproduced with permission from the American Chemical Society^{74,78,79,84}. **(c, i)** are reproduced with permission from Elsevier^{75,87}. **(d)** is reproduced with permission from Wiley⁷⁷.

and even some noble-metal-free alternatives⁷⁵. The corrosion resistance and stability can be attributed to low atomic diffusion, another core-effect of high-entropy systems^{22,76}. In HEMs, the “sluggish-diffusion” effect slows down the overall kinetics of atomic motion and phase transformation, which enhances structural integrity and corrosion resistance²⁹. Another example is the phosphorus-modified amorphous high-entropy CoFe-NiCrMn compound (2023), developed by one-step electrodeposition on nickel foam, with remarkable HER and hydrazine oxidation reaction (HzOR) performance: the overpotentials are as low as 51 and 268 mV at 100 mA cm⁻² for HER and HzOR, respectively. Elements like iron and nickel for HER and phosphorus and chromium for HzOR (Fig. 2d) contribute to lowering energy barriers and improving reaction kinetics⁷⁷. Morphology can also be carefully designed in HEMs to boost performance. NiCoFePtRh nanoparticles (2021) have been fabricated having an average diameter of 1.68 nm, achieving an ultrahigh mass activity of 28.3 A mg^{-1} at -0.05 V (vs. RHE) for HER in 0.5 M H_2SO_4 solution, 40.4 and 74.5 times higher than commercial Pt/C and Rh/C, respectively (Fig. 2e)⁷⁸. Likewise, CoCrFeNi (2021), a single-phase fcc system, shows an HER overpotential only 60 meV

larger than Pt at 1 mA cm⁻², but significantly better than pure Ni or stainless steel⁷⁹. HEMs also demonstrate improved catalytic activity and durability under the oxidative conditions of OER^{80–83}. NiFe and NiCoFe alloys are known for excellent OER activity, and additional non-noble-metal elements were incorporated to form high-entropy counterparts⁸⁴. AlNiCoFeX ($X = \text{Mo, Nb, Cr}$) (2019) exhibits a 240 mV overpotential and a 46 mV dec⁻¹ Tafel slope at 10 mA cm⁻² (Fig. 2g), attributed to its higher oxidation states enhancing oxygen adsorption on the surface. The incorporation of additional metal species has also proven to be an effective strategy for improving electrochemical durability over extended cycling periods (Fig. 2h).

Proton-exchange membrane (PEM) electrolysis is a promising technology for green hydrogen generation. However, its scale-up hinges on developing new highly active electrocatalysts that overcome the sluggish kinetics of OER under acidic conditions. Traditional OER electrocatalysts face three critical challenges: **(i)** the high operating potential required to drive OER in acidic environments (typically 1.8–2.2 V) accelerates corrosion and dissolution of the electrocatalysts, **(ii)** the strongly acidic environment promotes catalyst oxidation, leading to reduced electrocatalytic activity and

Fig. 3 | High-entropy materials in hydrogen-related applications. **a** Performance of various OER electrocatalysts at a current density of 10 mA cm^{-2} in $0.5 \text{ M H}_2\text{SO}_4$. The green dashed line indicates the lowest overpotential that can be achieved using non-precious metal catalysts. **b** Comparison of desorption temperature (K) and hydrogen storage capacity (wt%) for traditional metal hydrides and HEMs. A green band represents the typical operating temperature range for hydrogen fuel cells (60–90 °C). Data are available in Supplemental Table S.1 and S.2.



compromised long-term stability, and (iii) the reliance on rare and expensive noble metals has driven the scientific community to explore acid-stable OER electrocatalysts that minimize the use of these precious materials⁸⁵. Given their intrinsic properties, HEMs are emerging as ideal platforms to address these challenges. Figure 3a compares the performance of HEMs and traditional materials for OER applications under acidic conditions. For the catalysts without precious metals (blue rhombus), HEMs outperform traditional materials with lower overpotentials and lower Tafel slopes. Among them, CoFeNiMoWTe demonstrates one of the lowest combined overpotentials and Tafel slopes. The detailed performance and stability data for these materials are provided in Supplemental Table S.1.

Alongside experimental advancements, computational studies have played a key role in decoding and predicting the functionality of HEMs for hydrogen-related applications. For example, in $\text{Co}_{0.6}(\text{VMnNiZn})_{0.4}\text{PS}_3$ ⁷⁴, DFT was utilized to investigate hydrogen adsorption free energies and water-dissociation barriers, revealing that the Mn sites lower the Volmer-step barrier. Similarly, research on NiCoFePtRh nanoparticles⁷⁸ used DFT to map hydrogen-adsorption free energies (ΔG_{H^+}), demonstrating that the tailored electronic states of Pt and Rh reduce ΔG_{H^+} and desorption activation barriers. In another study on CoCrFeNi⁷⁹, DFT showed that partially oxidized surfaces enhance HER activity in acidic media by modifying surface reactivity, emphasizing that the elemental composition of the first nearest-neighbor shell strongly influences site reducibility (Fig. 2f). In the OER realm, density of state (DOS) calculations coupled with e_g orbital occupancy analysis identified dopant elements that optimize O-adsorbate binding energies⁸⁴. Beyond DFT, ML methods have emerged as powerful tools for high-throughput HEM discovery in hydrogen generation. Saidi et al.⁸⁶ combined DFT with a convolutional neural network (CNN) to screen over 4000 noble-metal-free compositions within the CoMoFeNiCu system for optimal hydrogen adsorption energies, helping the design of an alloy with adsorption properties comparable to Pt(111). DFT provided hydrogen adsorption energies and thermodynamic stability data (via enthalpy of mixing), which served as training inputs for the CNN. Additional ML models, such as random forest and gradient boosting, were evaluated, but the CNN proved to be the most accurate in capturing local chemical environments and complex composition-property relationships.

Fuel cells

The reverse reactions, hydrogen oxidation reaction (HOR) and oxygen reduction reaction (ORR), drive fuel cells generating electricity from hydrogen and oxygen. HOR occurs at the anode of fuel cells—where H_2 is oxidized to produce protons and electrons—while ORR takes place at the cathode where oxygen is reduced to water or other species, depending on the medium.

A quinary IrPdPtRhRu alloy (2019)⁸⁷ with a fcc structure exhibits an ORR overpotential roughly 20 mV lower than pure Pt(111) under comparable conditions. By fine-tuning the composition further, an optimized

variant, $\text{Ir}_{0.102}\text{Pd}_{0.320}\text{Pt}_{0.093}\text{Rh}_{0.196}\text{Ru}_{0.289}$, demonstrates a ~ 40 mV lower overpotential compared to Pt(111). Meanwhile, fcc PdNiRuIrRh (2023)⁸⁸ achieves an alkaline HOR mass activity of $3.25 \text{ mA } \mu\text{g}^{-1}$ —eight times higher than that of Pt/C. This enhancement is driven by tailored Pd-Pd-Ni/Pd-Pd bonding environments that improve ${}^2\text{H}$ adsorption, with oxophilic Ru or Ni further promoting water activation.

Computational studies have been crucial for understanding these remarkable fuel-cell performances and guiding HEM design. For IrPdPtRhRu alloys (2019)⁸⁷, a theoretical model was developed to predict the absorption spectra for ORR intermediates identifying the most active sites for HEMs. The adsorption energies of ${}^2\text{OH}$ on a random subset of possible binding sites were calculated by DFT and then used to train a ML model to predict the full span of adsorption energies on HEM surfaces (Fig. 2i). The model resolved a near-continuous spectrum of energies, indicating that the catalytic activity can be tailored through specific HEM compositions. In 2023, a study employed an ML-potential-based Monte Carlo simulation to explore how local coordination environments shift under operating conditions in a PdNiRuIrRh system, revealing the specific atomic cluster responsible for the eightfold activity enhancement over Pt/C⁸⁸.

Table 2 summarizes several studies applying ML to investigate HEMs for catalysis.

Hydrogen storage

Essential to enabling a hydrogen-based energy economy is the development of safe, effective, and scalable solutions for its storage. If a practical storage solution can be achieved, hydrogen can act as a type of “green battery” to help address the intermittency issues of other renewable energy sources. It can be generated and stored using excess renewable energy, then released during times of low supply and high demand, ensuring a stable and reliable energy grid⁸⁹. Hydrogen is an excellent candidate for such an application, having a three times higher energy density than traditional fossil fuels⁹⁰.

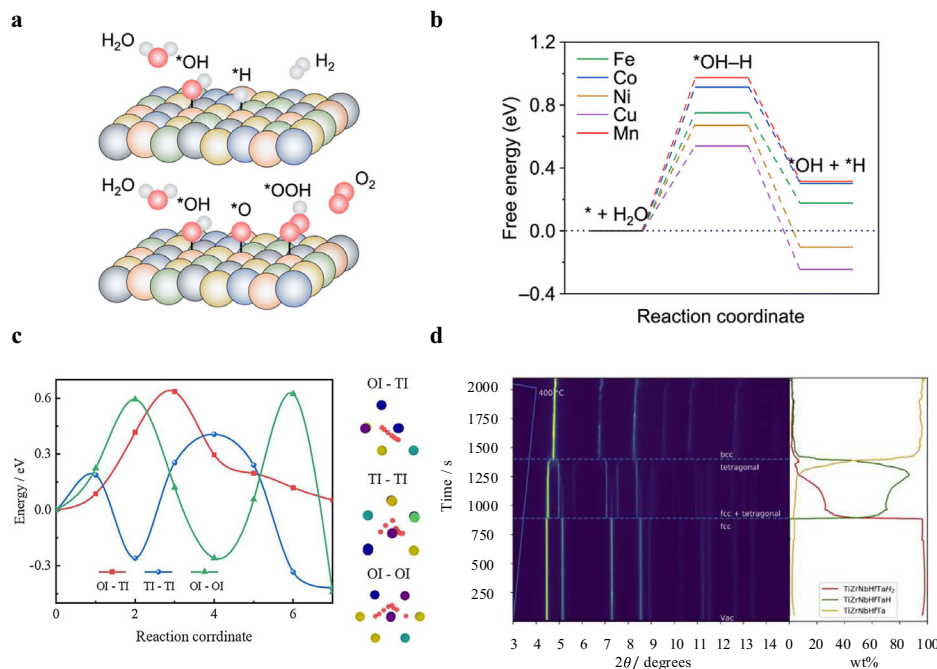
Traditional storage materials face several limitations, including low hydrogen-to-metal atom ratios and desorption processes demanding high temperatures for prolonged periods⁹¹: about 590 K for MgH_2 ⁹² and 673 K for NaBH_4 (Fig. 3b)⁹³. Stability is another challenge, with conventional materials undergoing degradation over multiple cycles of hydrogen absorption and desorption, resulting in lower capacities over time⁹⁴. Repeat cycling results in particle agglomeration and sintering in MgH_2 and the formation of intermediate phases in NaAlH_4 (for example Na_3AlH_6 and NaH), leading to a reduction in effective reaction surface area and incomplete reaction reversibility⁹⁴. Safety concerns remain a barrier: high-pressure (up to 700 bar) and cryogenic (liquid hydrogen) storage methods pose the risk of leaks and explosions⁹⁵.

HEMs have been designed to address several of these limitations. First, for hydrogen to be absorbed into the material, it must initially be adsorbed to the surface. The random atomic decorations in HEMs result in a large surface

Table 2 | Predicting catalytic properties of high-entropy materials with machine learning

Year	Composition	Application	Modeling approach	Ref.
2024	Mo-Cr-Mn-Fe-Co-Ni-Cu-Zn	Nitrogen reduction reaction in aqueous environments	Deep neural networks	350
2023	PdNiRuRh	Alkaline hydrogen oxidation reaction	Monte Carlo simulations using machine learning potentials	88
2023	PtPdRhAgCo, PtPdRuAgCo, PtPdRhAgFe, PtPdRuAgFe, PtPdRuAgNi	Water-gas shift reaction	Gaussian process regression	351
2024	ZnTe-MgTe-CaTe-S-Se	Photocatalytic water splitting	Secure independence screening and sparsifying operator	352
2024	(CoFeMnCuNiCr) ₃ O ₄	Solvent-free aerobic oxidation of benzyl alcohol	Adaptive boosting, categorical boosting, random forest, extreme gradient boosting	353
2023	Ag-Ir-Pd-Pt-Ru	Oxygen reduction reaction	Gaussian process regression	354
2024	CoCuGaNiZn, AgAuCuPdPt	CO ₂ and CO reduction reaction	Gaussian process regression	355
2024	CoMoFeNiCu	Hydrogen evolution reaction	Convolutional neural network, random forest, decision tree, gradient boosted decision tree	356
2024	CoMoFeNiCu	Ammonia decomposition reaction	XGBoost, machine learning force fields	86
2024	Fe-Co-Ni-Ru	Enhanced oxygen evolution reaction, hydrogen evolution reaction, and CO ₂ reduction reaction	Support vector machine	357
2024	FeCoNiCuMo	CO ₂ reduction reaction	Neural network	173
2024	FeCoNiCuZn	Nitrate adsorption for reduction to ammonia	Random forest regression, gradient boosting regression, AdaBoost regression, extra trees regression	358

Fig. 4 | Hydrogen storage. **a** Illustration of hydrogen and oxygen adsorption onto a high-entropy surface⁹⁸. **b** Gibbs free energy (ΔG_{H}^*) profiles for water dissociation on FeCoNiCuMn nanoparticles, resolved at distinct sites and specified by site centers⁹⁸. **c** Hydrogen diffusion pathways in FeCo-NiCrMn, where red, blue, and green lines represent pathways between octahedral interstitials (OI) and tetrahedral interstitials (TI), TI-TI, and OI-OI, respectively¹⁰². **d** In situ synchrotron radiation X-ray diffraction ($\lambda = 0.2071 \text{ \AA}$) and phase content during hydrogen desorption of TiZrNbHfTa in dynamic vacuum¹⁰⁴. (**a, b**) are reproduced with permission from Royal Society of Chemistry⁹⁸. (**c, d**) are reproduced with permission from Elsevier^{102,104}.



area and numerous distinct active sites, offering multiple reaction pathways and thus enhancing the kinetics^{96,97}. Moreover, the random coordinations convert otherwise inactive species into highly active reaction centers, as demonstrated for Cu in FeCoNiCuMn nanoparticles (2023) (Fig. 4a)⁹⁸. While monometallic Cu is inactive for both HER and OER, DFT calculations reveal that Cu sites in fcc FeCoNiCuMn nanoparticles possess the lowest energy barrier for water dissociation ($\Delta G_{\text{H}_2\text{O}}^* \rightarrow \Delta G_{\text{OH}}^*$), outperforming Fe, Co, Ni, and Mn sites (Fig. 4b). The site's high activity is attributed to electron donations from lower-electronegativity species (Mn, Fe, Co), driving competitive adsorption. Other studies have shown that elements such as palladium, known for its excellent hydrogen adsorption properties, can be effectively incorporated into HEMs to enhance surface interactions^{99,100}.

Once hydrogen molecules are adsorbed onto the surface, they dissociate into atoms and begin to diffuse into the bulk of the material. The varied atomic environments of HEMs provide a large number of interstitial sites of different shapes and sizes, creating various pathways that allow hydrogen atoms to migrate efficiently through the material¹⁰¹. Local lattice distortions—a result of these varying atomic environments and another core-effect of high entropy²²—further facilitate the trapping and release of hydrogen atoms. However, the diffusion process is not straightforward in HEMs. Diffusion pathways for hydrogen atoms in fcc FeCoNiCrMn (2021) have been calculated with DFT: the energy barriers span a wide range from 0.17 to 1.05 eV, indicating a more complex energy landscape compared to pure metals (Fig. 4c)¹⁰². The incorporation of elements such as zirconium,

vanadium, and niobium has also been shown to further enhance hydrogen absorption kinetics by creating more favorable pathways for diffusion¹⁰³.

Microstructural features—such as grain boundaries, defects, and phase interfaces—are influenced by high entropy and also strongly affect hydrogen diffusion within the material. A combined theoretical and experimental investigation of TiZrNbHfTa (2018) revealed that phase transformations in this system improved hydrogen storage capacity by providing stable sites for hydrogen incorporation and efficient pathways for diffusion¹⁰⁴. These phase transformations were monitored in reverse (i.e. during hydrogen desorption) using in-situ synchrotron radiation X-ray diffraction (Fig. 4d). The fully hydrogenated TiZrNbHfTa system exists as a fcc dihydride phase. An increase in temperature triggers an initial release of hydrogen and the nucleation of a secondary tetragonal monohydride phase. Continued desorption reduces the relative content of the original dihydride phase and leads to a contraction of the *c*-axis in the secondary monohydride phase. Eventually, the alloy transitions to its preferred dehydrogenated state: a body-centered cubic (bcc) crystal. Enhanced hydrogen diffusion has also been demonstrated in MgAlTiFeNi, which rapidly releases all its hydrogen on the order of a few seconds and at temperatures 100 °C lower than that of commercial MgH₂¹⁰⁵. ML algorithms have been employed to predict hydrogen absorption and release capacities in HEMs, facilitating their discovery and optimization for hydrogen storage¹⁰⁶. A DFT-informed, multi-objective Bayesian optimization framework was developed to screen candidate systems and led to the discovery of eight new HEMs¹⁰⁷. Among these, bcc VNbCrMoMn (2024) exhibits exceptional capacity, storing 2.83 wt% hydrogen at room temperature and ambient pressure, surpassing that of state-of-the-art LaNi₅H₆ and TiFeH₂, which store 1.38 and 1.91 wt% hydrogen, respectively.

Figure 3b plots the hydrogen storage capacity as a function of the desorption temperature. HEMs demonstrate a significant advantage at lower desorption temperatures (**blue area**). In many applications, such as portable hydrogen storage and backup power systems, reducing reliance on additional heating improves overall energy efficiency. Furthermore, since many hydrogen fuel cells operate at moderate temperatures (e.g., PEM fuel cells at 50–80 °C), the ability of HEMs to efficiently release hydrogen within this range eliminates the need for complex heating mechanisms and enhances performance.

Batteries

Next-generation batteries are rapidly being developed to enable electric vehicles, energy storage systems, the aerospace industry, and autonomous electric devices^{108–111}. Among these, (i) lithium-ion batteries possess high energy densities, high coulombic efficiencies, and low self-discharge^{112,113}; (ii) lithium-sulfur batteries are being investigated for increasing energy densities^{114–116}; and (iii) solid-state batteries offer a promising solution for the flammable and toxic organic liquid electrolyte in batteries¹¹⁷. However, battery materials face several challenges hindering their energy and power densities, including sluggish ion transport kinetics during (de)intercalation, limited structure stability/cyclability, and a low-voltage discharging plateau of their cathode materials. A high-entropy design has been shown to effectively address these limitations. As with high-entropy catalysts, the multi-element composition of high-entropy batteries enables tailored electrochemical behavior¹¹⁸. Furthermore, through the stabilization of new and unique elemental mixtures, HEMs offer a promising pathway for reducing reliance on critical elements, a persistent challenge for these ubiquitous energy storage systems. HEMs have been investigated as battery electrodes, chemical anchors of polysulfides in lithium-sulfur batteries, and the electrolyte in solid-state batteries. In 2019, a rhombohedral-structured compound, NaNi_{0.12}Cu_{0.12}Mg_{0.12}Fe_{0.15}Co_{0.15}Mn_{0.1}Ti_{0.1}Sn_{0.1}Sb_{0.04}O₂, was prepared and applied as a cathode material for sodium-ion batteries. The material exhibits impressive stability and rate capability, retaining 83% of its capacity after 500 cycles and maintaining 80% capacity retention at a charge-discharge rate of 5.0 C¹¹⁹. In 2021, rocksalt Li_{1.3}Mn_{0.1}Co_{0.1}Mn_{0.1}Cr_{0.1}Ti_{0.1}Nb_{0.2}O_{1.7}F_{0.3} (space group *Fm*³*m*) was synthesized and applied as a cathode material for lithium-ion batteries. The material demonstrates rapid lithium-ion transport, 40%

greater specific energy than lower entropy counterparts, a superior discharge capacity of > 170 mAh g⁻¹ when cycled at a current of 2 A g⁻¹, and long-term cycling stability¹²⁰. In 2023, high-entropy solid-state electrolyte Li_{5.5}PS_{4.5}Cl_{0.8}Br_{0.7} (space group *F43m*) was reported to have an outstanding ionic conductivity of 22.7 mS cm⁻¹ at room temperature, resulting in stable cycling over 700 cycles with minimal capacity degradation¹²¹. Most recently, in 2024, nano Pt_{0.25}Cu_{0.25}Fe_{0.15}Co_{0.15}Ni_{0.2} with a fcc structure was synthesized and integrated into the sulfur cathode. The pouch cell with this composite cathode achieves a high capacity retention of 71.3% after 43 cycles at 0.1 C¹²².

DFT calculations are valuable tools for exploring battery materials¹²³, especially in understanding the underlying mechanisms of HEMs in batteries. Band structure and DOS calculations show reduced bandgaps in HEMs (e.g., Fig. 5a), which enhances the electronic conductivity of the electrodes and promotes reaction kinetics^{124–128}. Ionic migration path models reveal both lower barriers and final state energies in HEMs (Fig. 5b)¹²⁴. Lower barriers boost ionic conductivity, while lower final state energies suppress atomic site rearrangements and corresponding phase transition processes in low-voltage zones—enhancing the overall energy density. Differential charge density diagrams (Fig. 5c) demonstrate stronger electron interactions in HEMs, illustrating efficient adsorption and transfer of ions¹²⁷. DFT calculations also indicate that high-entropy anodes experience a smaller volume expansion with lithium-ion incorporation, improving cyclability (Fig. 5d)¹²⁶. For Li-S battery systems, major challenges include the sluggish and complex phase transition of sulfur species during electrochemical reactions, the electrical insulating nature of lithium polysulfides (LiPS) and sulfur, and the “shuttle” effect depleting active material from the cathode—resulting in less cycling stability and reduced coulombic efficiency^{114,129,130}. Sulfur-hosted HEMs address these issues. HEMs have shown higher binding energies and smaller bond distances (Fig. 5e), indicating stronger interactions and better affinities to LiPS than samples with single metal species. Enhanced electron transfer in HEMs during LiPS transformations have been further confirmed by analyses of the Bader charges and charge density difference contours¹²². HEMs therefore serve as an anchor to restrain LiPS via chemical confinement, as well as a catalyst for redox reactions in the cathodes¹¹⁴.

Electronics

Semiconductors are the foundation of modern electronic and photonic devices, forming the basis of transistors, diodes, and photovoltaic cells¹³¹. No industry is under as much demand, with metal-oxide-semiconductor field-effect transistors (MOSFETs) being the most numerous produced artificial objects in history¹³². While effective, traditional materials such as Si and Ge are reaching their physical limits, particularly in the context of Moore’s Law, which predicts the doubling of transistors on a microchip every two years¹³³.

As transistors are becoming smaller, issues such as quantum tunneling, heat generation, and electron scattering become more pronounced, limiting the performance and reliability of semiconductor devices¹³⁴. Additionally, emerging semiconductor-based technologies such as energy storage¹³⁵, thermoelectric materials¹³⁶, photocatalysis¹³⁷, and advanced photovoltaic systems¹³⁸ demand materials with superior performance, i.e. higher carrier mobility, thermal stability, and mechanical strength¹³⁹.

In response to these challenges, HEMs have been adopted as a solution. By tailoring element combinations in HEMs, researchers can optimize bandgaps, carrier concentrations, and defect densities to enhance semiconductor performance^{140,141}, enabling more efficient, reliable, and versatile devices for energy conversion, storage, catalysis, CO₂ reduction, and beyond (Table 3)^{142,143}.

Photovoltaics

Photovoltaic devices such as solar cells have become popular for passive and sustainable energy generation, especially as they have become more manufacturable. However, several challenges, including limited efficiency and durability constrain their broader application^{144–146}. Through compositional-tuning, HEMs have been designed to have bandgaps that absorb a

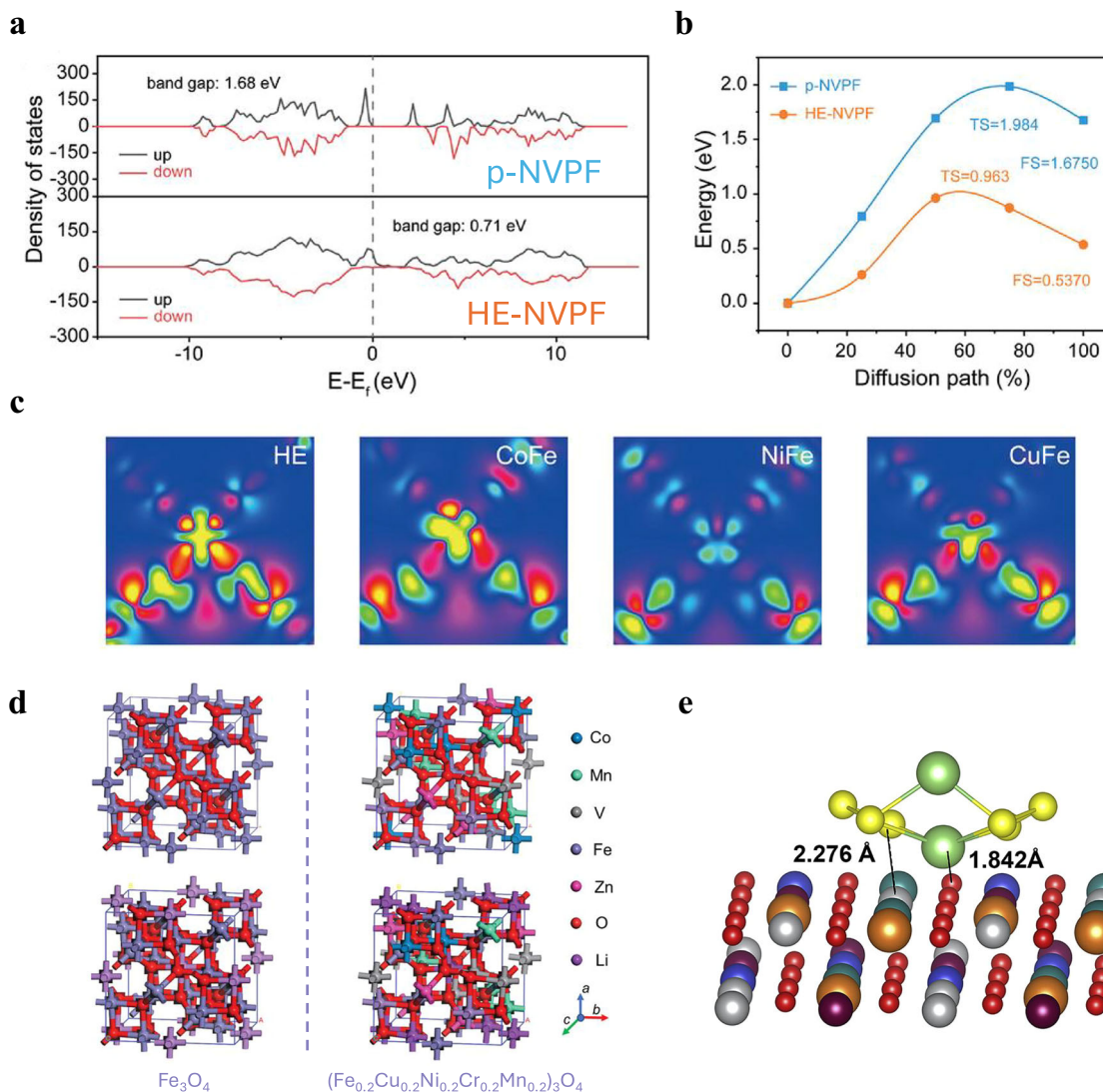


Fig. 5 | Batteries. **a** Density of states plot for cathode materials in sodium ion batteries: pristine $\text{Na}_3\text{V}_2(\text{PO}_4)_2\text{F}_3$ (p-NVPF) and high-entropy NVPF (HE-NVPF)¹²⁴. **b** The migration energy profile of p-NVPF and HE-NVPF¹²⁴. **c** Difference charge-density maps of conventional and high-entropy Prussian blue analogues¹²⁷. **d** Structural models of Fe_3O_4 and high-entropy spinel

$(\text{Co}_{0.2}\text{Mn}_{0.2}\text{V}_{0.2}\text{Fe}_{0.2}\text{Zn}_{0.2})_3\text{O}_4$ before (up) and after (down) incorporating the same amount of lithium-ions. Corresponding volume expansion rates can then be calculated¹²⁶. **e** Geometry configuration of Li_2S_6 binding to high-entropy oxide ($\text{MgCoNiCuZn})\text{O}$ ¹¹⁴. **(a-d)** are reproduced with permission from Wiley^{124,126,127}. **(e)** is reproduced with permission from Elsevier¹¹⁴.

broader spectrum of sunlight, enhancing their efficiencies¹⁴⁷. High-throughput screening of rare-earth fluorite-type oxides, most of which exhibit a fluorite structure ($Fm\bar{3}m$) while others exhibit a bixbyite structure ($Ia\bar{3}$), reveal a range of bandgaps spanning 2.0 eV ($(\text{CeSmPrY})\text{O}_2$) to 4.9 eV ($(\text{CeLaSmYZr})\text{O}_2$) (2023)¹⁴⁸. These materials exhibit both high electron mobility and appropriate energy levels for solar cell integration, demonstrating utility for various light absorption applications.

Photocatalysis

The reduction of CO_2 into valuable hydrocarbons and fuels is critical for addressing climate change and developing sustainable energy systems. High-entropy oxide TiZrNbHfTaO_{11} (2022), with various structural defects, exhibits enhanced photocatalytic activity for the conversion of CO_2 to CO and H_2O to H_2 ¹⁴⁹. Its superior efficiency compared to traditional catalysts like TiO_2 and BiVO_4 is due to lattice strain and oxygen vacancies which improve charge separation and reduce electron-hole recombination. Additionally, the multi-cation composition enhances light absorption across a broad spectrum, while the dual-phase structure improves charge carrier mobility. HEMs also show promise in other photocatalytic applications, such as environmental remediation and pollutant degradation.

Rare-earth high entropy oxides have been explored in photocatalytic degradation of organic pollutants¹⁵⁰, exhibiting bandgaps ranging from 1.91 to 3.0 eV and demonstrating exceptional photocatalytic activity.

Thermoelectrics

Thermoelectric materials present a promising waste-heat recovery solution, converting a temperature differential into electricity and vice versa. The maximum efficiency achievable by a thermoelectric at a given temperature is determined by the dimensionless figure of merit, $zT = S^2 \sigma T / \kappa$, where S is the Seebeck coefficient, σ is the electrical conductivity, T is the absolute temperature, and κ is the thermal conductivity¹⁵¹. zT depends on both electronic transport (S and σ) and thermal transport properties (κ) of a material, with the optimal thermoelectric having high electronic conductivity and low thermal conductivity. The intrinsically counter-correlated behavior between electronic and thermal transport properties makes the enhancement of zT a very challenging task¹⁵².

HEMs offer a new path in the design of thermoelectric materials. Increased zT values can be achieved through disorder-driven enhanced phonon scattering and lattice distortions, compositionally-optimized carrier concentrations, and electronic band structures. This was accomplished in a

Table 3 | Applications of high-entropy semiconducting materials

Year	Field	Material	Description	Ref.
2022	Energy storage	$[(\text{K}_{0.2}\text{Na}_{0.8})_{0.8}\text{Li}_{0.08}\text{-Ba}_{0.02}\text{Bi}_{0.1}]$ $(\text{Nb}_{0.68}\text{Sc}_{0.02}\text{-Hf}_{0.08}\text{Zr}_{0.1}\text{Ta}_{0.08}\text{Sb}_{0.04}\text{O}_3)$	Lead-free energy storage capacitor achieving a giant recoverable energy density of 10.06 J cm^{-3} with an ultrahigh efficiency of 90.8%	359
2022	Energy storage	$(\text{Bi}_{3.25}\text{La}_{0.75})(\text{Ti}_{3-x}\text{Zr}_x\text{-Hf}_x\text{Sn}_x)\text{O}_{12}$	High-energy density capacitor achieving an energy density of 182 J cm^{-3} with an efficiency of 78% at an electric field of 6.35 MV cm^{-1}	360
2024	Energy storage	$\text{Li}_x(\text{MgCoNiCuZn})\text{O}$	Improved electrical conductivity across a wide range of temperatures (79–773 K) and pressures (up to 50 GPa), suitable for Li-ion battery applications under extreme conditions	361
2019	Optoelectronics	SiGeSn	Narrowed bandgap of 0.38 eV and local lattice distortions with low vacancy formation energies due to bond reformation	362
2023	Optoelectronics	$(\text{La}_{0.2}\text{Ce}_{0.2}\text{Nd}_{0.2}\text{-Gd}_{0.2}\text{Bi}_{0.2})_2\text{Ti}_2\text{O}_7$	Efficient photo-detection capabilities with a bandgap of 3.16 eV, excellent stability with only 5% attenuation in photocurrent after 6 months	363
2021	Photocatalysis	$\text{TiZrHfNbTaO}_6\text{N}_3$	Narrowed bandgap of 1.6 eV coupled with excellent stability	364
2022	Photocatalysis	TiZrNbHTaO_{11}	Improved photocatalytic activity for CO_2 conversion attributed to unique dual-phase structure, lattice defects, and efficient charge carrier dynamics	149
2022	Photocatalysis	$(\text{Co,Cu,Mg,Ni,Zn})\text{O}$	Tunable bandgap ranging from 1.47 to 3.38 eV, suitable for visible light harvesting and photocatalytic applications	365
2023	Photocatalysis	$(\text{Ca}_x\text{ZrYCeCr}_x)\text{O}_2$	Enhanced piezo-photocatalytic activity at 38 at% Ca, attributed to prolonged carrier lifetimes and efficient charge separation induced by ferroelectric polarization	366
2016	Thermoelectrics	$(\text{BiSbTe}_{1.5}\text{Se}_{1.5})_{1-x}\text{-Ag}_x$	Reduced lattice thermal conductivity of $0.47 \text{ W m}^{-1}\text{K}^{-1}$ at 400 K due to severe lattice distortions, achieving a peak zT of 0.63 at 450 K with the addition of 0.9 at% Ag	214
2017	Thermoelectrics	PbSnTeSe	Reduced lattice thermal conductivity of less than $0.6 \text{ W m}^{-1}\text{K}^{-1}$ at room temperature and a peak zT of 0.8 at 873 K due to severe lattice distortions after 1.5% La doping	214
2018	Thermoelectrics	$\text{Cu}_3\text{SnMgInZnS}_7$	Reduced lattice thermal conductivity and single-phase stability	158
2020	Thermoelectrics	$\text{Sr}(\text{Ti}_{0.2}\text{Fe}_{0.2}\text{Mo}_{0.2}\text{-Nb}_{0.2}\text{Cr}_{0.2})\text{O}_3$	Low lattice thermal conductivity of $0.7 \text{ W m}^{-1}\text{K}^{-1}$ at 1100 K due to enhanced electron-phonon and Umklapp scattering	154
2020	Thermoelectrics	AgSnSbSe_3	Low lattice thermal conductivity of $0.47 \text{ W m}^{-1}\text{K}^{-1}$ at 673 K due to cation disorder and phonon anharmonicity, achieves a peak zT of 1.14 at 723 K with Te alloying	155
2021	Thermoelectrics	$\text{Cu}_{0.8}\text{Ag}_{0.2}(\text{ZnGe})_{0.1}\text{-}(\text{GaIn})_{0.4}\text{Te}_2$	Low thermal conductivity of $0.51 \text{ W m}^{-1}\text{K}^{-1}$ and a peak zT of 1.02 at 820 K	157
2021	Thermoelectrics	$\text{Pb}_{0.935}\text{Na}_{0.025}\text{Cd}_{0.04}\text{-Se}_{0.5}\text{S}_{0.25}\text{Te}_{0.25}$	Low lattice thermal conductivity of $0.33 \text{ W m}^{-1}\text{K}^{-1}$ and a peak zT of 2.0 at 900 K, due to band convergence and hierarchical structures that scatter heat-carrying phonons	160
2021	Thermoelectrics	$\text{Sn}_{0.25}\text{Pb}_{0.25}\text{Mn}_{0.25}\text{-Ge}_{0.25}\text{Te}$	Low lattice thermal conductivity and an enhanced zT of 1.52 at 823 K, achieved through enhanced phonon scattering	156
2021	Thermoelectrics	AgMnGeSbTe_4	Low lattice thermal conductivity of $0.54 \text{ W m}^{-1}\text{K}^{-1}$ at 300 K and a peak zT of 1.27 at 773 K resulting from lattice distortions and band convergence	367
2022	Thermoelectrics	$\text{AgMnSn}_{0.25}\text{Pb}_{0.75}\text{-SbTe}_4$	High-entropy alloy with a reduced lattice thermal conductivity of $0.54 \text{ W m}^{-1}\text{K}^{-1}$ and a peak zT of 1.3 at 773 K, achieved through lattice distortions and band convergence	260
2022	Thermoelectrics	$\text{Sr}_{0.9}\text{La}_{0.1}(\text{Zr}_{0.25}\text{-Sn}_{0.25}\text{Ti}_{0.25}\text{Hf}_{0.25})\text{O}_3$	Low thermal conductivity of 1.89 W/mK and a high Seebeck coefficient of $393 \mu\text{V/K}$ at 873 K	368
2022	Thermoelectrics	$\text{Ge}_{0.61}\text{Ag}_{0.11}\text{Sb}_{0.13}\text{-Pb}_{0.12}\text{Bi}_{0.01}\text{Te}$	Reduced lattice thermal conductivity of $0.3 \text{ W m}^{-1}\text{K}^{-1}$ and a peak zT of 2.7 at 750 K by tuning electron and phonon localization	159

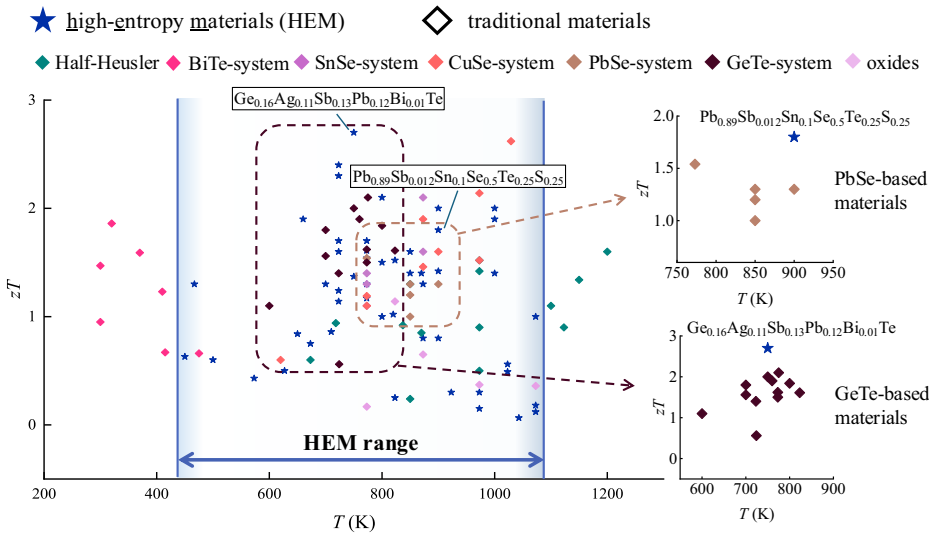
high-entropy PbSe-based system $\text{Pb}_{0.89}\text{Sb}_{0.012}\text{Sn}_{0.1}\text{Se}_{0.5}\text{Te}_{0.25}\text{S}_{0.25}$ (2021) with a rocksalt structure reported to have a zT of 1.8 at 900 K—higher than other PbSe-based materials¹⁵³ (Fig. 6). Similarly, the high-entropy perovskite $\text{Sr}(\text{Ti}_{0.2}\text{Fe}_{0.2}\text{Mo}_{0.2}\text{-Nb}_{0.2}\text{Cr}_{0.2})\text{O}_3$ (2020) with a $Pm\bar{3}m$ space group demonstrates reduced lattice thermal conductivity due to enhanced phonon scattering from the introduction of five multivalent cations at the B site. This design reduces the phonon mean free path from 0.8 nm at room temperature to 0.5 nm at 1100 K, lowering the thermal conductivity to $0.7 \text{ W m}^{-1}\text{K}^{-1}$ at 1100 K¹⁵⁴. High thermoelectric performance has been achieved in high-entropy rocksalt $\text{AgSnSbSe}_{1.5}\text{Te}_{1.5}$ (2020), with a peak zT of 1.14 at 723 K and an average of about 1.0 over a wide temperature range of 400–773 K—nearly double the performance of AgSnSbSe_3 (peak zT of 0.65 and an average of about 0.47). This is driven by Se/Te anion disorder, which introduces additional point defects and dislocations, enhancing phonon scattering and effectively reducing the lattice thermal conductivity to $0.32 \text{ W m}^{-1}\text{K}^{-1}$ at 723 K, thereby improving thermoelectric performance¹⁵⁵.

Figure 6 provides a comprehensive comparison of thermoelectric performances as a function of temperature for traditional materials and HEMs. HEMs are clustered in the mid-temperature region (highlighted in blue), where they exhibit a higher average zT than traditional materials of the same material family. Among them, $\text{Ge}_{0.61}\text{Ag}_{0.11}\text{Sb}_{0.13}\text{Pb}_{0.12}\text{Bi}_{0.01}\text{Te}$, a

GeTe-based HEM, achieves the highest zT , surpassing conventional GeTe-based thermoelectric materials. Together with other high-performance examples, it exemplifies the potential of high-entropy engineering in optimizing thermoelectric performance through compositional tuning.

The band structure and DOS provide insights into the enhanced electronic and thermoelectric properties of HEMs. By capturing changes in lattice parameters, orbital hybridization, and defect states, computational modeling reveals the mechanisms through which alloying and compositional tuning optimize carrier transport. In SnTe-based HEMs, DFT studies reveal that alloying with Pb, Ge, and Mn promotes valence-band convergence, thus increasing the effective carrier mass and the Seebeck coefficient. For instance, rocksalt structure $\text{Sn}_{0.25}\text{Pb}_{0.25}\text{Mn}_{0.25}\text{Ge}_{0.25}\text{Te}$ (2021) achieves a peak zT of 1.52 at 823 K, owing to carefully engineered band structures and minimized defect scattering¹⁵⁶. Meanwhile, $\text{Cu}_{0.8}\text{Ag}_{0.2}(\text{ZnGe})_{0.1}\text{-}(\text{GaIn})_{0.4}\text{Te}_2$ (2021) exhibits pronounced lattice distortions at Cu sites—influencing the valence band edge dominated by Cu- d and Te- p orbitals—leading to an improved zT of 1.02 at 820 K. This high-entropy design reduced the thermal conductivity of CuInTe_2 by more than 80%. DFT calculations indicate that substitutions at Cu sites can balance the trade-off between carrier scattering and low thermal conductivity, resulting in

Fig. 6 | High-entropy materials in thermoelectric materials. Comparison of thermoelectric performance zT as a function of temperature for traditional materials and HEMs. The right-side subfigures highlight specific systems with HEMs for better visualization. Related data are provided in Supplemental Table S.3.



improved thermoelectric efficiency¹⁵⁷. In high-entropy sulfides, such as Cu₅SnMgGeZnS₉ (2018), DOS analyses highlight the stabilization of complex phases via configurational entropy. By revealing Cu-3d and S-3p states near the valence-band maximum, these calculations link local strain reduction to enhanced phase stability and moderate thermoelectric performance¹⁵⁸.

Phonon transport plays a pivotal role in determining the thermoelectric performance of HEMs. Computational methods have helped unveil the mechanisms by which entropy-driven lattice dynamics and structural complexity enhance thermoelectric efficiency. In high-entropy GeTe-based systems, Ge_{0.61}Ag_{0.11}Sb_{0.03}Pb_{0.12}Bi_{0.01}Te (2022) simulations reveal the dual role of entropy in delocalizing electron distributions and localizing phonons. The calculated charge density maps show that increased crystal symmetry reduces electron localization, promoting band convergence and enhancing electrical transport properties. Simultaneously, entropy-induced disorder enhances anharmonicity, suppressing transverse phonon modes and leading to significantly reduced lattice thermal conductivity. These computational insights align with experimental observations of a high zT of 2.7 at 750 K¹⁵⁹. For Cd-doped p-type chalcogenides Pb_{0.935}Na_{0.025}Cd_{0.04}Se_{0.5}S_{0.25}Te_{0.25} (2021), theoretical models provide a mechanistic understanding of how alloying tunes both electronic and thermal transport. DFT studies demonstrate that lattice distortions induced by Cd doping enhance phonon scattering while maintaining a stable electronic transport framework. The calculations also reveal that hierarchical nanostructures and entropy-stabilized matrices synergistically reduce lattice thermal conductivity while optimizing the Seebeck coefficient and carrier mobility, contributing to a zT value of 2.0 at 900 K¹⁶⁰.

Biofuels

Significant effort has been invested in producing valuable liquid fuels and chemicals from biomass feedstock. Biomass—which is abundant, renewable, and globally available^{161–163}—primarily consists of hemicellulose, lignin, and cellulose^{164,165}. The quality of furfural-based biofuels, produced from hemicellulose, depends on the length of its carbon chains, which can be extended through oxidative condensation reactions with aliphatic alcohols. These reactions cannot be performed with excessive heat, and developing catalyst systems operating at mild temperatures remains a significant challenge. In 2023, a non-noble-metal-based HEM, MgLaFeMnCu, featuring a spinel phase structure (space group $F\bar{d}3m$), demonstrated exceptional catalytic performance. As illustrated in Fig. 7e, this catalyst synthesized C7 to C17 fuel precursors at ambient temperatures, significantly outperforming conventional systems in operational efficiency and energy

requirements¹⁶⁶. Similarly, lignin, the second largest component of renewable biomass, is an essential source for biofuel. However, the pyrolysis of lignin typically results in high-oxygen content products that, when used as biofuels, suffer from low energy density, unstable combustion, and excessive corrosion. The selective removal of oxygen from natural lignocellulosic materials is critical for producing biofuels^{167,168}. To address this issue, the hetero-structured catalyst NiZnCuFeAl/NiZnCuFeAlZrO_x with $F\bar{d}3m$ symmetry was developed in 2024¹⁶⁹. As shown in Fig. 7f, g, it exhibits exceptional catalytic performance, achieving 100% vanillin conversion and 95% selectivity for the high-value product 2-methyl-4-methoxy phenol at just 120°C, maintaining efficiency even after five cycles. For MgLaFeMnCu, the exceptional catalytic performance is attributed to the abundance of oxygen vacancies, high surface area, and synergistic effects of the numerous metallic components¹⁶⁶. Likewise, the NiZnCuFeAl/NiZnCuFeAlZrO_x heterostructure leverages its high-entropy oxide matrix to provide excellent hydrogenolysis capabilities and robust electron transfer pathways. The synergistic effects of the alloy and oxide components further ensure selective oxygen removal, high chemoselectivity, and catalyst durability over multiple cycles¹⁶⁹. These advancements underscore the transformative potential of HEMs in sustainable biofuel production.

Challenges and future direction

One of the most promising aspects of HEMs—their compositional complexity offering enhanced and emergent properties—can also be a barrier to their discovery and optimization.

For hydrogen generation and storage, this complexity makes it difficult to tune stability, adsorption energies/absorption capacities, and release kinetics simultaneously^{29,170}. The high configurational entropy that stabilizes these materials can also lead to unwanted phases or structural heterogeneity, which may degrade performance over multiple cycles of hydrogen absorption and desorption^{29,171}. From a computational perspective, the compositional complexity of HEMs also presents obstacles to their design. For example, classical transition state theory (TST) has been immensely helpful in modeling catalytic processes on uniform metal surfaces, especially in conjunction with scaling and Brønsted-Evans-Polanyi (BEP) relations. These frameworks quantify the Sabatier principle by linking adsorption energies of key intermediates (such as *OH and *OOH) to reaction barriers, making it straightforward to pinpoint “ideal” adsorption energies for high catalytic activity. However, TST is challenging to apply to HEMs because each surface site can have a unique local composition. In more complex reactions—e.g., involving multiatom adsorption sites—the transition state may interact with different surface atoms than those in the initial and final states. Enumerating each unique configuration and reaction pathway in

HEMs exceeds the practical limits of TST¹⁷². In recent years, ML has emerged as a powerful tool for this problem. ML models trained on DFT/experimental data can capture the vast configuration space of HEM surfaces, enabling the prediction of adsorption energies and reaction barriers across a diverse range of surface sites¹⁷³. By bypassing the reliance on predefined scaling relations like BEP, ML can directly map local atomic environments to kinetic parameters, accounting for the unique geometries and chemistries of individual sites on HEMs. Additionally, ML-driven approaches can provide insights into the statistical distribution of active sites and their catalytic performance, identifying high-probability pathways for efficient reactions without explicitly enumerating all possible configurations¹⁷⁴. Despite these advancements, HEM surfaces—having unusual compositions and complex geometries—pose a distinct challenge for ML-based approaches, which strongly rely on high-fidelity and representative training data. Dealing with larger, more complex reaction networks while maintaining accuracy remains computationally expensive and requires significant algorithmic innovation.

For high-entropy batteries, further research is needed to understand the mechanisms driving the enhanced performance. Although the properties of HEMs can be customized through the cocktail effect, the customization process is mostly random. A significant challenge is identifying functional units and understanding the roles of individual elements. Future studies should aim to incorporate elements with lower redox potentials, thereby reducing lithiation voltages¹⁷⁵. There is some debate as to whether

changing the anions can enhance the energy efficiencies¹⁷⁵. The relationship between voltage hysteresis and the anion properties is not yet well understood, encouraging further investigation. Another challenge is the minimal application of HEMs in industrially-relevant battery materials¹⁷⁶. Scale-up beyond the laboratory level is both cost-prohibitive and technically challenging; scalable synthesis methods are currently being investigated^{177–179}.

For biofuel synthesis, HEM stability and performance can be improved, especially following the high temperature treatment required for biomass conversion. The synthesis process with HEMs is complex, hindering scalability and industrial application. As with hydrogen generation/storage, the multi-element composition makes it difficult to achieve the right balance of catalytic activity, selectivity, and durability. Catalyst deactivation is also a frequent issue at high temperatures, and chemical contaminants can poison active sites or lead to coking and sintering.

A key concern for the thermal and phase stability of HEMs is that entropy-driven stabilization, while beneficial at elevated temperatures, may not entirely suppress phase separation and undesired transformations under extreme operating conditions. In ceramics, for instance, additional doping and tailored composition gradients can bolster single-phase stability¹⁸⁰. *In-operando* characterization will play a vital role in studying HEMs, revealing transient phase changes and localized segregation. From the modeling side, thermodynamic integration, advanced Monte Carlo sampling, and ML force fields offer the ability to capture finite-temperature and kinetic effects with fewer computational

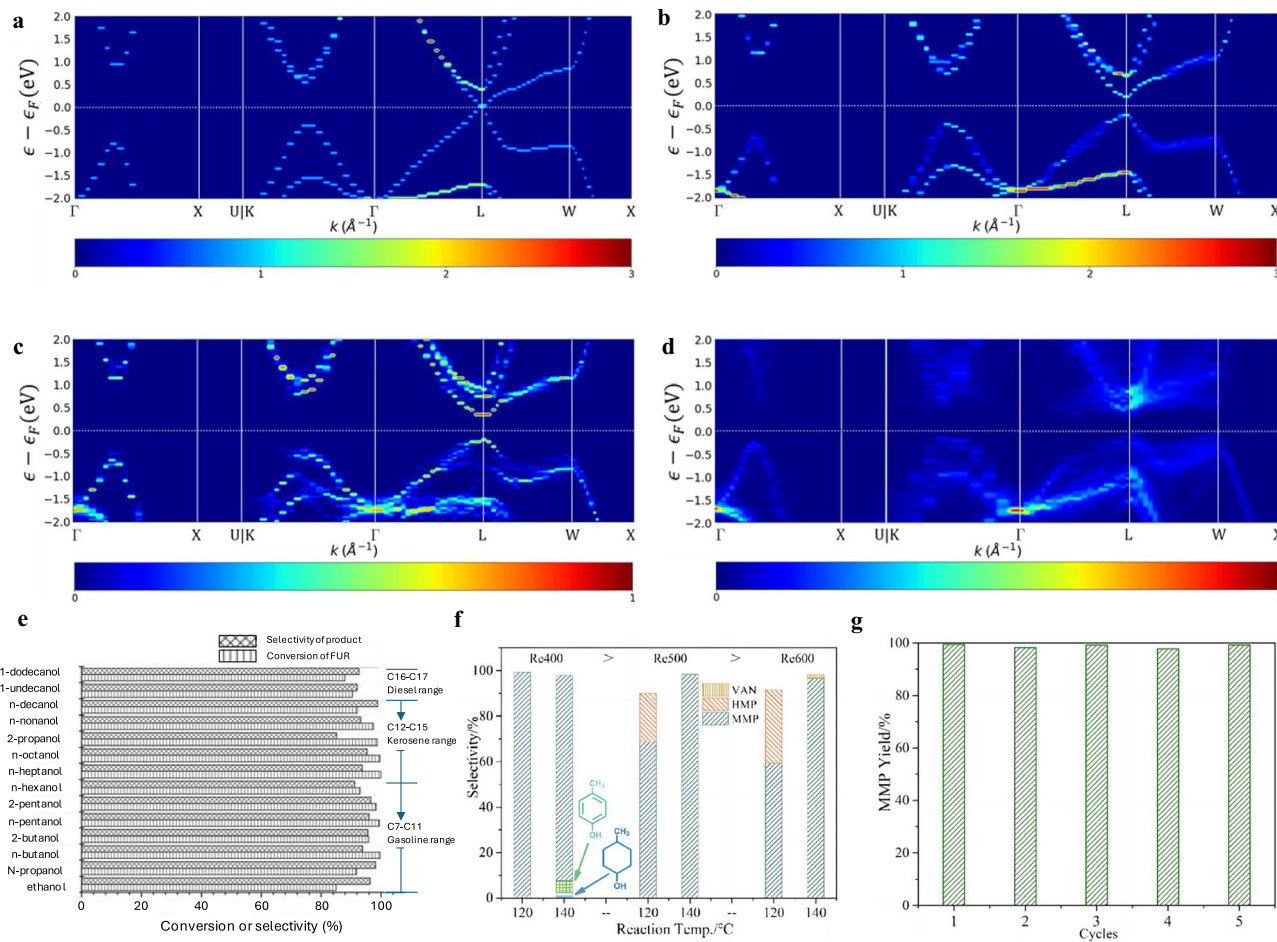


Fig. 7 | Thermoelectrics and biofuels. Band structures of SnTe-based alloys: a $\text{Sn}_{32}\text{Te}_{32}$, b $(\text{Sn}_{16}\text{Pb}_{16})\text{Te}_{32}$, c $(\text{Sn}_9\text{Pb}_9\text{Ge}_9)\text{Te}_{27}$, and d $(\text{Sn}_8\text{Pb}_8\text{Mn}_8\text{Ge}_8)\text{Te}_{32}$ ¹⁵⁶. e Synthesis of C₇–C₁₇ fuel precursors via oxidative condensation reactions of furfural with different aliphatic alcohols mediated by high-entropy catalyst MgLaFeMnCu¹⁶⁶. f Products distribution of hetero-structured high-entropy catalysts prepared at 400 °C (Re400), 500 °C (Re500), and 600 °C (Re600) and at reaction temperatures of 120/140 °C¹⁶⁹. Products VAN is vanillin, HMP is 4-hydroxymethyl-2-methoxyphenol, and MMP is 2-methyl-4 methoxy phenol. g Stability test of hetero-structured high-entropy catalyst Re400, measuring product MMP yield across repeated reaction cycles¹⁶⁹. (a–e) are reproduced with permission from American Chemical Society^{156,166}. (f, g) are reproduced with permission from Wiley¹⁶⁹.

140 °C¹⁶⁹. Products VAN is vanillin, HMP is 4-hydroxymethyl-2-methoxyphenol, and MMP is 2-methyl-4 methoxy phenol. g Stability test of hetero-structured high-entropy catalyst Re400, measuring product MMP yield across repeated reaction cycles¹⁶⁹. (a–e) are reproduced with permission from American Chemical Society^{156,166}. (f, g) are reproduced with permission from Wiley¹⁶⁹.

bottlenecks. Deploying these tools more systematically can reveal compositional “safe zones” that balance enthalpic and entropic factors to maintain solid-solution behavior.

Given the multi-element nature of HEMs, compositional tuning has been a central focus for the field, and much remains unexplored. The next frontier includes examination of synthesis pathways and processing parameters and how they also govern formation, properties, and scalability of these systems¹⁸¹. New synthesis methods achieving higher effective temperatures¹⁸² will help realize previously-inaccessible HEMs with distinct and exotic properties^{35,183}. HEM synthesis methods also need to be optimized for industrial application, considering production cost, speed/automation, and quality. Varying processing parameters like annealing times, heating rates, and pressure can dramatically affect the microstructure and morphology, enabling optimization of properties that span multiple scales like hardness and electrical/thermal conductivities^{175,184–188}. Integrating computational and data-driven approaches with experiments is essential to elucidating and navigating these complex processing-structure-property relationships. Computational-experimental feedback loops will, with each iteration, improve the accuracy of the models and direct resources to the most fruitful candidates. Progress in high-throughput calculations/modeling—already capable of predicting thermodynamic synthesizability and functional properties—will focus on resolving manufacturability through the prediction of formation temperatures, kinetics, surface interactions, and material lifetime/degradation processes. Capturing these features ab initio is essential to boosting the technology readiness level of this relatively new class of materials.

Conclusion

A high-entropy design has proven to be transformative in the development of green energy solutions, offering a versatile platform for advanced materials with tailored properties. The blend of elements in HEMs—which was previously inaccessible for some chemistries—allows for unprecedented control over material behavior, leading to enhancements in performance above and beyond the state-of-the-art across various energy technologies^{85,153–157,159,160,189–342}. However, challenges remain, particularly in deconvolving the disorder-driven dynamics within HEMs that would enable systematic design and optimization for each specific application. The complexity of the search space and of the interactions within HEMs calls for more advanced computational tools that can uncover the underlying mechanisms and guide the design/discovery of even better performing HEMs. A critical next step is deploying multi-scale modeling approaches, combining DFT for accurate local electronic structures, generating ML force fields for large-scale simulations, performing Monte Carlo for sampling accessible configurations, and constructing thermodynamic databases focused on HEMs. High-throughput frameworks and ML/AI-based screening can accelerate the discovery of new compositions with targeted properties. Kinetic modeling beyond standard TST—accounting for local site disorder—can reveal reaction pathways that are otherwise unavailable on uniform metal surfaces. On the synthesis side, upcoming methods must reconcile scalability, cost-effectiveness, and quality control to bridge the gap between laboratory-scale development and industrial production. Techniques that achieve higher effective temperatures (e.g., laser-assisted sintering and plasma-based processes) can unlock previously inaccessible phases with unique and advanced functionalities. Microwave plasma chemical vapor deposition, arc melting, and mechanical alloying—extended to near- or super-equiautomatic conditions—are among the promising routes for rapid, large-scale fabrication. Careful control over annealing and cooling rates can fine-tune the microstructure, promoting homogeneous single-phase HEMs and multiphase architectures with well-controlled interfaces. Integrated computational-experimental feedback loops³⁴³—where virtual materials are experimentally validated and experimental data refines predictive models—offer a powerful engine to streamline research toward industry-ready HEMs. Disorder-by-design will continue to lead the charge toward a more sustainable, green-energy-powered future.

Data availability

No datasets were generated or analyzed during the current study.

Received: 7 November 2024; Accepted: 1 April 2025;

Published online: 22 May 2025

References

1. Creutzig, F. et al. The underestimated potential of solar energy to mitigate climate change. *Nat. Energy* **2**, 17140 (2017).
2. Gielen, D., Boshell, F. & Saygin, D. Climate and energy challenges for materials science. *Nat. Mater.* **15**, 117–120 (2016).
3. Gielen, D. et al. The role of renewable energy in the global energy transformation. *Energy Strategy Rev.* **24**, 38–50 (2019).
4. Chu, S., Cui, Y. & Liu, N. The path towards sustainable energy. *Nat. Mater.* **16**, 16–22 (2017).
5. U.S. Energy Information Administration (EIA). *International Energy Outlook 2021 Narrative*. https://www.eia.gov/outlooks/ieo/pdf/IEO2021_Narrative.pdf (2021). (Accessed 28 October 2024).
6. Kuzemko, C. & Bradshaw, M. *Energy Security: Geopolitics, Governance and Multipolarity* 22–43 (Springer, 2013).
7. Zhao, D. et al. Modeling the Nexus between geopolitical risk, oil price volatility and renewable energy investment; evidence from Chinese listed firms. *Renew. Energy* **225**, 120309 (2024).
8. Logadóttir, H. H. & the United Nations, *Iceland's Sustainable Energy Story: A Model for the World?*. <https://www.un.org/en/chronicle/article/icelands-sustainable-energy-story-model-world> (2015). (Accessed 3 September 2024).
9. International Trade Administration, U.S. Department of Commerce, *Energy Resource Guide—Renewable Energy—Costa Rica*. <https://www.trade.gov/energy-resource-guide-renewable-energy-costarica> (2024). (Accessed 3 September 2024).
10. Oses, C., Toher, C. & Curtarolo, S. Data-driven design of inorganic materials with the automatic flow framework for materials discovery. *MRS Bull.* **43**, 670–675 (2018).
11. Chu, S. & Majumdar, A. Opportunities and challenges for a sustainable energy future. *Nature* **488**, 294–303 (2012).
12. George, E. P., Raabe, D. & Ritchie, R. O. High-entropy alloys. *Nat. Rev. Mater.* **4**, 515–534 (2019).
13. Oses, C., Toher, C. & Curtarolo, S. High-entropy ceramics. *Nat. Rev. Mater.* **5**, 295–309 (2020).
14. Amiri, A. & Shahbazian-Yassar, R. Recent progress of high-entropy materials for energy storage and conversion. *J. Mater. Chem. A* **9**, 782–823 (2021).
15. Wu, L. & Hofmann, J. P. High-entropy transition metal chalcogenides as electrocatalysts for renewable energy conversion. *Curr. Opin. Electrochem.* **34**, 101010 (2022).
16. Ma, J. & Huang, C. High entropy energy storage materials: synthesis and application. *J. Energy Storage* **66**, 107419 (2023).
17. Deng, C., Wang, T., Wu, P., Zhu, W. & Dai, S. High entropy materials for catalysis: a critical review of fundamental concepts and applications. *Nano Energy* **120**, 109153 (2023).
18. Yang, K., Oses, C. & Curtarolo, S. Modeling off-stoichiometry materials with a high-throughput ab-initio approach. *Chem. Mater.* **28**, 6484–6492 (2016).
19. Rost, C. M. et al. Entropy-stabilized oxides. *Nat. Commun.* **6**, 8485 (2015).
20. Sarker, P. et al. High-entropy high-hardness metal carbides discovered by entropy descriptors. *Nat. Commun.* **9**, 4980 (2018).
21. Cantor, B., Chang, I. T. H., Knight, P. & Vincent, A. J. B. Microstructural development in equiautomatic multicomponent alloys. *Mater. Sci. Eng. A* **375–377**, 213–218 (2004).
22. Yeh, J.-W. et al. Nanostructured high-entropy alloys with multiple principle elements: novel alloy design concepts and outcomes. *Adv. Eng. Mater.* **6**, 299–303 (2004).

23. Huang, E.-W. et al. Machine-learning and high-throughput studies for high-entropy materials. *Mater. Sci. Eng. R* **147**, 100645 (2022).
24. Wang, Q., Velasco, L., Breitung, B. & Presser, V. High-entropy energy materials in the age of big data: a critical guide to next-generation synthesis and applications. *Adv. Energy Mater.* **11**, 2102355 (2021).
25. Li, J., Fang, Q. & Liaw, P. K. Microstructures and properties of high-entropy materials: modeling, simulation, and experiments. *Adv. Eng. Mater.* **23**, 2001044 (2021).
26. Kaufmann, K. et al. Discovery of high-entropy ceramics via machine learning. *npj Comput. Mater.* **6**, 42 (2020).
27. Oses, C. et al. aflow++: A C++ framework for autonomous materials design. *Comput. Mater. Sci.* **217**, 111889 (2023).
28. Lokhande, V., Malavekar, D., Kim, C., Vinu, A. & Ji, T. Order within disorder: unveiling the potential of high entropy materials in energy storage and electrocatalysis. *Energy Storage Mater.* **72**, 103718 (2024).
29. Hsu, W.-L., Tsai, C.-W., Yeh, A.-C. & Yeh, J.-W. Clarifying the four core effects of high-entropy materials. *Nat. Rev. Chem.* **8**, 471–485 (2024).
30. Zhao, S. Application of machine learning in understanding the irradiation damage mechanism of high-entropy materials. *J. Nucl. Mater.* **559**, 153462 (2022).
31. Oses, C. et al. AFLOW-CHULL: cloud-oriented platform for autonomous phase stability analysis. *J. Chem. Inf. Model.* **58**, 2477–2490 (2018).
32. Esters, M. et al. Settling the matter of the role of vibrations in the stability of high-entropy carbides. *Nat. Commun.* **12**, 5747 (2021).
33. Brahlek, M. et al. What is in a name: defining “high entropy” oxides. *APL Mater.* **10**, 110902 (2022).
34. Rosenberg, W., Ness, S. C., Mishra, B., Segre, C. U. & McCormack, S. J. Excess thermochemical properties and local structure in the entropy stabilized (Hf-Zr)TiO₄ system. *Acta Mater.* **285**, 120639 (2025).
35. Divilov, S. et al. Disordered enthalpy-entropy descriptor for high-entropy ceramics discovery. *Nature* **625**, 66–73 (2024).
36. Wang, D. et al. Spinel-structured high entropy oxide (FeCoNiCrMn)₃O₄ as anode towards superior lithium storage performance. *J. Alloys Compd.* **844**, 156158 (2020).
37. Lökçü, E., Toparlı, C. & Anık, M. Electrochemical performance of (MgCoNiZn)_{1-x}Li_xO high-entropy oxides in lithium-ion batteries. *ACS Appl. Mater. Inter.* **12**, 23860–23866 (2020).
38. Yan, J. et al. A high-entropy perovskite titanate lithium-ion battery anode. *J. Mater. Sci.* **55**, 6942–6951 (2020).
39. Cheng, W. et al. Pressure-stabilized high-entropy (FeCoNiCuRu)S₂ sulfide anode toward simultaneously fast and durable lithium/sodium ion storage. *Small* **19**, 2301915 (2023).
40. Li, F., Zhou, L., Liu, J.-X., Liang, Y. & Zhang, G.-J. High-entropy pyrochlores with low thermal conductivity for thermal barrier coating materials. *J. Adv. Ceram.* **8**, 576–582 (2019).
41. Li, X. et al. Rapid synthesis of high entropy perovskite oxides with oxygen vacancies at high pressure for thermoelectric applications. *Ceram. Int.* **50**, 15144–15158 (2024).
42. Kim, J. H. et al. Enhancement of critical current density and strong vortex pinning in high entropy alloy superconductor Ta_{1/6}Nb_{2/6}Hf_{1/6}Zr_{1/6}Ti_{1/6} synthesized by spark plasma sintering. *Acta Mater.* **232**, 117971 (2022).
43. Teng, Z. et al. Reactive spark plasma sintering of high-entropy (La_{1/7}Nd_{1/7}Sm_{1/7}Eu_{1/7}Gd_{1/7}Dy_{1/7}Ho_{1/7})₂Zr₂O₇ pyrochlore ceramic. *Ceram. Int.* **50**, 6892–6897 (2024).
44. Qiao, H. et al. Scalable synthesis of high entropy alloy nanoparticles by microwave heating. *ACS Nano* **15**, 14928–14937 (2021).
45. Maulana, A. L. et al. Understanding the structural evolution of IrFeCoNiCu high-entropy alloy nanoparticles under the acidic oxygen evolution reaction. *Nano Lett.* **23**, 6637–6644 (2023).
46. Minouei, H. et al. Rapid microwave-assisted synthesis and magnetic properties of high-entropy spinel (Cr_{0.2}Mn_{0.2}Fe_{0.2}Co_{0.2-x}Ni_{0.2}Zn_x)₃O₄ nanoparticles. *Ceram. Int.* **49**, 11885–11892 (2023).
47. Yen, J.-Z., Yang, Y.-C. & Tuan, H.-Y. Interface engineering of high entropy Oxide@Polyaniline heterojunction enables highly stable and excellent lithium ion storage performance. *Chem. Eng. J.* **450**, 137924 (2022).
48. Nguyen, T. X. et al. Secondary-phase-induced charge-discharge performance enhancement of Co-free high entropy spinel oxide electrodes for Li-ion batteries. *Adv. Func. Mater.* **33**, 2300509 (2023).
49. Patra, J. et al. Effects of elemental modulation on phase purity and electrochemical properties of co-free high-entropy spinel oxide anodes for lithium-ion batteries. *Adv. Func. Mater.* **32**, 2110992 (2022).
50. Qian, L. et al. Towards low-voltage and high-capacity conversion-based oxide anodes by configuration entropy optimization. *ChemElectroChem* **10**, e202201012 (2023).
51. Ustinov, A. I. et al. Effect of structure of high entropy CrFeCoNiCu alloys produced by EB PVD on their strength and dissipative properties. *J. Alloys Compd.* **887**, 161408 (2021).
52. Hossain, M. D. et al. Entropy landscaping of high-entropy carbides. *Adv. Mater.* **33**, 2102904 (2021).
53. Su, J. et al. High entropy oxide nanofiber by electrospun method and its application for lithium battery anode material. *Int. J. Appl. Ceram. Technol.* **19**, 2004–2015 (2022).
54. Triolo, C. et al. Charge storage mechanism in electrospun spinel-structured high-entropy (Mn_{0.2}Fe_{0.2}Co_{0.2}Ni_{0.2}Zn_{0.2})₃O₄ oxide nanofibers as anode material for Li-ion batteries. *Small* **19**, 2304585 (2023).
55. Zunger, A., Wei, S.-H., Ferreira, L. G. & Bernard, J. E. Special quasirandom structures. *Phys. Rev. Lett.* **65**, 353–356 (1990).
56. Esters, M. et al. QH-POCC: taming tiling entropy in thermal expansion calculations of disordered materials. *Acta Mater.* **245**, 118594 (2023).
57. Hollingsworth, S. A. & Dror, R. O. Molecular dynamics simulation for all. *Neuron* **99**, 1129–1143 (2018).
58. Hart, G. L. W., Mueller, T., Toher, C. & Curtarolo, S. Machine learning and alloys. *Nat. Rev. Mater.* **6**, 730–755 (2021).
59. Unke, O. T. et al. Machine learning force fields. *Chem. Rev.* **121**, 10142–10186 (2021).
60. van de Walle, A. & Asta, M. D. Self-driven lattice-model Monte Carlo simulations of alloy thermodynamic properties and phase diagrams. *Model. Simul. Mater. Sci. Eng.* **10**, 521 (2002).
61. Lee, J. & Kosterlitz, J. M. Finite-size scaling and Monte Carlo simulations of first-order phase transitions. *Phys. Rev. B* **43**, 3265 (1991).
62. Panagiotopoulos, A. Z. Direct determination of phase coexistence properties of fluids by Monte Carlo simulation in a new ensemble. *Mol. Phys.* **61**, 813–826 (1987).
63. Wallace, S. K., Frost, J. M. & Walsh, A. Atomistic insights into the order-disorder transition in Cu₂ZnSnS₄ solar cells from Monte Carlo simulations. *J. Mater. Chem. A* **7**, 312–321 (2019).
64. Feng, R. et al. High-throughput design of high-performance lightweight high-entropy alloys. *Nat. Commun.* **12**, 4329 (2021).
65. Esters, M. et al. aflow.org: a web ecosystem of databases, software and tools. *Comput. Mater. Sci.* **216**, 111808 (2023).
66. Jain, A. et al. A high-throughput infrastructure for density functional theory calculations. *Comput. Mater. Sci.* **50**, 2295–2310 (2011).
67. Saal, J. E., Kirklin, S., Aykol, M., Meredig, B. & Wolverton, C. Materials design and discovery with high-throughput density functional theory: The Open Quantum Materials Database (OQMD). *JOM* **65**, 1501–1509 (2013).
68. Singh, M., Barr, E. & Aidhy, D. Consolidated database of high entropy materials (COD'HEM): an open online database of high entropy materials. *Comput. Mater. Sci.* **248**, 113588 (2025).

69. Andersson, J.-O., Helander, T., Höglund, L., Shi, P. & Sundman, B. Thermo-Calc & DICTRA, computational tools for materials science. *Calphad* **26**, 273–312 (2002).
70. Bak, T., Nowotny, J., Rekas, M. & Sorrell, C. C. Photo-electrochemical hydrogen generation from water using solar energy. Materials-related aspects. *Int. J. Hydrogen Energy* **27**, 991–1022 (2002).
71. Benghanem, M. et al. Hydrogen production methods based on solar and wind energy: a review. *Energies* **16**, 757 (2023).
72. Ursua, A., Gandia, L. M. & Sanchis, P. Hydrogen production from water electrolysis: current status and future trends. *Proc. IEEE* **100**, 410–426 (2011).
73. Usharani, N. J., Shringi, R., Sanghavi, H., Subramanian, S. & Bhattacharya, S. S. Role of size, alio-/multi-valency and non-stoichiometry in the synthesis of phase-pure high entropy oxide (Co, Cu, Mg, Na, Ni, Zn) O. *Dalton Trans.* **49**, 7123–7132 (2020).
74. Wang, R. et al. Two-dimensional high-entropy metal phosphorus trichalcogenides for enhanced hydrogen evolution reaction. *ACS Nano* **16**, 3593–3603 (2022).
75. Zhang, G. et al. High entropy alloy as a highly active and stable electrocatalyst for hydrogen evolution reaction. *Electrochim. Acta* **279**, 19–23 (2018).
76. Miracle, D. B. High-entropy alloys: a current evaluation of founding ideas and core effects and exploring “nonlinear alloys”. *JOM* **69**, 2130–2136 (2017).
77. Li, K. et al. Phosphorus-modified amorphous high-entropy CoFeNiCrMn compound as high-performance electrocatalyst for hydrazine-assisted water electrolysis. *Small* **19**, 2302130 (2023).
78. Feng, G. et al. Sub-2 nm ultrasmall high-entropy alloy nanoparticles for extremely superior electrocatalytic hydrogen evolution. *J. Am. Chem. Soc.* **143**, 17117–17127 (2021).
79. McKay, F. et al. CoCrFeNi high-entropy alloy as an enhanced hydrogen evolution catalyst in an acidic solution. *J. Phys. Chem. C* **125**, 17008–17018 (2021).
80. Huang, K. et al. Exploring the impact of atomic lattice deformation on oxygen evolution reactions based on a sub-5 nm pure face-centred cubic high-entropy alloy electrocatalyst. *J. Mater. Chem. A* **8**, 11938–11947 (2020).
81. Cui, X., Zhang, B., Zeng, C. & Guo, S. Electrocatalytic activity of high-entropy alloys toward oxygen evolution reaction. *MRS Commun.* **8**, 1230–1235 (2018).
82. Waag, F. et al. Kinetically-controlled laser-synthesis of colloidal high-entropy alloy nanoparticles. *RSC Adv.* **9**, 18547–18558 (2019).
83. Jin, S. Are metal chalcogenides, nitrides, and phosphides oxygen evolution catalysts or bifunctional catalysts? *ACS Energy Lett.* **8**, 1937–1938 (2017).
84. Qiu, H.-J. et al. Noble metal-free nanoporous high-entropy alloys as highly efficient electrocatalysts for oxygen evolution reaction. *ACS Mater. Lett.* **1**, 526–533 (2019).
85. Zhu, H. et al. High-entropy alloy stabilized active Ir for highly efficient acidic oxygen evolution. *Chem. Eng. J.* **431**, 133251 (2022).
86. Saidi, W. A., Nandi, T. & Yang, T. Designing multinary noble metal-free catalyst for hydrogen evolution reaction. *Electrochem. Sci. Adv.* **3**, e2100224 (2023).
87. Batchelor, T. A. A. et al. High-entropy alloys as a discovery platform for electrocatalysis. *Joule* **3**, 834–845 (2019).
88. Men, Y. et al. Understanding alkaline hydrogen oxidation reaction on PdNiRuIrRh high-entropy-alloy by machine learning potential. *Angew. Chem. Int. Ed.* **62**, e202217976 (2023).
89. Rivard, E., Trudeau, M. & Zaghib, K. Hydrogen storage for mobility: a review. *Materials* **12**, 1973 (2019).
90. Zhang, F., Zhao, P., Niu, M. & Maddy, J. The survey of key technologies in hydrogen energy storage. *Int. J. Hydrogen Energy* **41**, 14535–14552 (2016).
91. Sakintuna, F., Lamari-Darkrim, B. & Hirscher, M. Metal hydride materials for solid hydrogen storage: a review. *Int. J. Hydrogen Energy* **32**, 1121–1140 (2007).
92. Sun, Z. et al. Realizing hydrogen de/absorption under low temperature for MgH₂ by doping Mn-based catalysts. *Nanomater.* **10**, 1745 (2020).
93. Dragan, M. Hydrogen storage in complex metal hydrides NaBH₄: hydrolysis reaction and experimental strategies. *Catalysts* **12**, 356 (2022).
94. Thongtan, P. et al. Reversible hydrogen sorption and kinetics of hydrogen storage tank based on MgH₂ modified by TiF₄ and activated carbon. *Int. J. Hydrogen Energy* **43**, 12260–12270 (2018).
95. Züttel, A. Hydrogen storage methods. *Naturwissenschaften* **91**, 157–172 (2004).
96. Wang, Y. et al. Synergistic effect between undercoordinated platinum atoms and defective nickel hydroxide on enhanced hydrogen evolution reaction in alkaline solution. *Nano Energy* **48**, 590–599 (2018).
97. Sivanantham, A. et al. Complementary functions of vanadium in boosting electrocatalytic activity of CuCoNiFeMn high-entropy alloy for water splitting. *Adv. Func. Mater.* **33**, 2301153 (2023).
98. Zhu, H. et al. A high-entropy atomic environment converts inactive to active sites for electrocatalysis. *Energy Environ. Sci.* **16**, 619–628 (2023).
99. Savvotin, I. et al. Thermochemical analysis of hydrogenation of Pd-containing composite based on TiZrVNbTa high-entropy alloy. *Appl. Sci.* **13**, 9052 (2023).
100. Zaluski, L., Zaluska, A., Tessier, P., Ström-Olsen, J. O. & Schulz, R. Catalytic effect of Pd on hydrogen absorption in mechanically alloyed Mg₂Ni, LaNi₅ and FeTi. *J. Alloys Compd.* **217**, 295–300 (1995).
101. Marques, F., Balcerzak, M., Winkelmann, F., Zepon, G. & Felderhoff, M. Review and outlook on high-entropy alloys for hydrogen storage. *Energy Environ. Sci.* **14**, 5191–5227 (2021).
102. Xie, Z., Wang, Y., Lu, C. & Dai, L. Sluggish hydrogen diffusion and hydrogen decreasing stacking fault energy in a high-entropy alloy. *Mater. Today Commun.* **26**, 101902 (2020).
103. Zhang, J. et al. Superior Hydrogen Sorption Kinetics of Ti_{0.20}Zr_{0.20}Hf_{0.20}Nb_{0.40} High-Entropy Alloy. *Metals* **11**, 470 (2021).
104. Zlotea, C. et al. Hydrogen sorption in TiZrNbHfTa high entropy alloy. *J. Alloys Compd.* **775**, 667–674 (2019).
105. Cardoso, K. R. et al. Hydrogen storage in MgAlTiFeNi high entropy alloy. *J. Alloys Compd.* **858**, 158357 (2020).
106. Osman, A. I. et al. Enhanced hydrogen storage efficiency with sorbents and machine learning: a review. *Environ. Chem. Lett.* **22**, 1703–1740 (2024).
107. Halpren, E., Yao, X., Chen, Z. W. & Singh, C. V. Machine learning assisted design of BCC high entropy alloys for room temperature hydrogen storage. *Acta Mater.* **270**, 119841 (2024).
108. Lu, X. et al. Polymer-based solid-state electrolytes for high-energy-density lithium-ion batteries—review. *Adv. Energy Mater.* **13**, 2301746 (2023).
109. Yang, B. et al. Critical summary and perspectives on state-of-health of lithium-ion battery. *Renew. Sust. Energ. Rev.* **190**, 114077 (2024).
110. Ye, Y. et al. Ultralight and fire-extinguishing current collectors for high-energy and high-safety lithium-ion batteries. *Nat. Energy* **5**, 786–793 (2020).
111. Chen, H. et al. Free-standing ultrathin lithium metal-graphene oxide host foils with controllable thickness for lithium batteries. *Nat. Energy* **6**, 790–798 (2021).
112. Kim, T., Song, W., Son, D.-Y., Ono, L. K. & Qi, Y. Lithium-ion batteries: outlook on present, future, and hybridized technologies. *J. Mater. Chem. A* **7**, 2942–2964 (2019).

113. Nitta, N., Wu, F., Lee, J. T. & Yushin, G. Li-ion battery materials: present and future. *Mater. Today* **18**, 252–264 (2015).
114. Zheng, Y. et al. A high-entropy metal oxide as chemical anchor of polysulfide for lithium-sulfur batteries. *Energy Storage Mater.* **23**, 678–683 (2019).
115. Manthiram, A., Fu, Y., Chung, S.-H., Zu, C. & Su, Y.-S. Rechargeable lithium-sulfur batteries. *Chem. Rev.* **114**, 11751–11787 (2014).
116. Zhao, M., Li, B.-Q., Zhang, X.-Q., Huang, J.-Q. & Zhang, Q. A perspective toward practical lithium-sulfur batteries. *ACS Cent. Sci.* **6**, 1095–1104 (2020).
117. Sun, Y.-K. Promising all-solid-state batteries for future electric vehicles. *ACS Energy Lett.* **5**, 3221–3223 (2020).
118. Ouyang, B. & Zeng, Y. The rise of high-entropy battery materials. *Nat. Commun.* **15**, 973 (2024).
119. Zhao, C., Ding, F., Lu, Y., Chen, L. & Hu, Y.-S. High-entropy layered oxide cathodes for sodium-ion batteries. *Angew. Chem. Int. Ed.* **59**, 264–269 (2020).
120. Lun, Z. et al. Cation-disordered rocksalt-type high-entropy cathodes for Li-ion batteries. *Nat. Mater.* **20**, 214–221 (2021).
121. Li, S. et al. High-entropy lithium argyrodite solid electrolytes enabling stable all-solid-state batteries. *Angew. Chem. Int. Ed.* **62**, e202314155 (2023).
122. Han, F. et al. High-entropy alloy electrocatalysts bidirectionally promote lithium polysulfide conversions for long-cycle-life lithium-sulfur batteries. *ACS Nano* **18**, 15167–15176 (2024).
123. Zhang, T., Li, D., Tao, Z. & Chen, J. Understanding electrode materials of rechargeable lithium batteries via DFT calculations. *Prog. Nat. Sci.-Mater.* **23**, 256–272 (2013).
124. Gu, Z.-Y. et al. An advanced high-entropy fluorophosphate cathode for sodium-ion batteries with increased working voltage and energy density. *Adv. Mater.* **34**, 2110108 (2022).
125. Ran, B. et al. High entropy activated and stabilized nickel-based prussian blue analogue for high-performance aqueous sodium-ion batteries. *Energy Storage Mater.* **71**, 103583 (2024).
126. Hou, S. et al. Unlocking the origins of highly reversible lithium storage and stable cycling in a spinel high-entropy oxide anode for lithium-ion batteries. *Adv. Func. Mater.* **34**, 2307923 (2024).
127. Du, K. et al. High-entropy Prussian Blue analogues enable lattice respiration for ultra-stable aqueous aluminum-ion batteries. *Adv. Mater.* **36**, 2404172 (2024).
128. Ding, X. et al. A high-entropy-designed cathode with V^{5+} - V^{2+} multi-redox for high energy density sodium-ion batteries. *J. Energy Chem.* **97**, 429–437 (2024).
129. Liu, D. et al. Catalytic effects in lithium-sulfur batteries: promoted sulfur transformation and reduced shuttle effect. *Adv. Sci.* **5**, 1700270 (2018).
130. Huang, J.-Q., Zhang, Q. & Wei, F. Multi-functional separator/interlayer system for high-stable lithium-sulfur batteries: Progress and prospects. *Energy Storage Mater.* **1**, 127–145 (2015).
131. Aoki, K. et al. Microassembly of semiconductor three-dimensional photonic crystals. *Nat. Mater.* **2**, 117–121 (2003).
132. Laws, David 13 Sextillion & Counting: The Long & Winding Road to the Most Frequently Manufactured Human Artifact in History. <https://computerhistory.org/blog/13-sexillion-counting-the-long-winding-road-to-the-most-frequently-manufactured-hum> (2018). (Accessed 23 October 2024).
133. Waldrop, M. M. The chips are down for Moore's law. *Nature* **530**, 144 (2016).
134. Chhowalla, M., Jena, D. & Zhang, H. Two-dimensional semiconductors for transistors. *Nat. Rev. Mater.* **1**, 16052 (2016).
135. Garcia, N. G. et al. Medium-and high entropy materials as positive electrodes for sodium-ion batteries: Quo Vadis? *Energy Storage Mater.* **67**, 103213 (2024).
136. Tang, Q. et al. High-entropy thermoelectric materials. *Joule* **8**, 1641–1666 (2024).
137. Pan, Y., Liu, J.-X., Tu, T.-Z., Wang, W. & Zhang, G.-J. High-entropy oxides for catalysis: a diamond in the rough. *Chem. Eng. J.* **451**, 138659 (2023).
138. Crabtree, G. W. & Lewis, N. S. Solar energy conversion. *Physics Today* **60**, 37–42 (2007).
139. Li, S.-L., Tsukagoshi, K., Orgiu, E. & Samorí, P. Charge transport and mobility engineering in two-dimensional transition metal chalcogenide semiconductors. *Chem. Soc. Rev.* **45**, 118–151 (2016).
140. Dallaev, R., Spusta, T., Allaham, M. M., Spotz, Z. & Sobola, D. Synthesis and band gap characterization of high-entropy ceramic powders. *Crystals* **14**, 295 (2024).
141. Katzbauer, R. R., dos Santos Vieira, F. M., Dabo, I., Mao, Z. & Schaak, R. E. Band gap narrowing in a high-entropy spinel oxide semiconductor for enhanced oxygen evolution catalysis. *J. Am. Chem. Soc.* **145**, 6753–6761 (2023).
142. Shaikh, J. S. et al. High entropy materials frontier and theoretical insights for logistics CO_2 reduction and hydrogenation: electrocatalysis, photocatalysis and thermo-catalysis. *J. Alloys Compd.* **969**, 172232 (2023).
143. Das, S., Chowdhury, S. & Tiwary, C. S. High-entropy-based nanomaterials for sustainable environmental applications. *Nanoscale* **16**, 8256–8272 (2024).
144. Johnston, M. B. & Herz, L. M. Hybrid perovskites for photovoltaics: charge-carrier recombination, diffusion, and radiative efficiencies. *Acc. Chem. Res.* **49**, 146–154 (2016).
145. Shi, R. et al. Structural disorder in higher-temperature phases increases charge carrier lifetimes in metal halide perovskites. *J. Am. Chem. Soc.* **144**, 19137–19149 (2022).
146. Rajagopal, A., Stoddard, R. J., Jo, S. B., Hillhouse, H. W. & Jen, A. K.-Y. Overcoming the photovoltage plateau in large bandgap perovskite photovoltaics. *Nano Lett.* **18**, 3985–3993 (2018).
147. Prasanna, R. et al. Band gap tuning via lattice contraction and octahedral tilting in perovskite materials for photovoltaics. *J. Am. Chem. Soc.* **139**, 11117–11124 (2017).
148. Kumbhakar, M. et al. High-throughput screening of high-entropy fluorite-type oxides as potential candidates for photovoltaic applications. *Adv. Energy Mater.* **13**, 2204337 (2023).
149. Akrami, S. et al. Defective high-entropy oxide photocatalyst with high activity for CO_2 conversion. *Appl. Catal. B* **303**, 120896 (2022).
150. Nundy, S. et al. Bandgap engineering in novel fluorite-type rare earth high-entropy oxides (RE-HEOs) with computational and experimental validation for photocatalytic water splitting applications. *Adv. Sustainable Syst.* **6**, 2200067 (2022).
151. Ioffe, A. F. et al. Semiconductor thermoelements and thermoelectric cooling. *Physics Today* **12**, 42 (1959).
152. Shi, X., Chen, L. & Uher, C. Recent advances in high-performance bulk thermoelectric materials. *Int. Mater. Rev.* **61**, 379–415 (2016).
153. Jiang, B. et al. High-entropy-stabilized chalcogenides with high thermoelectric performance. *Science* **371**, 830–834 (2021).
154. Banerjee, R. et al. High-entropy perovskites: an emergent class of oxide thermoelectrics with ultralow thermal conductivity. *ACS Sustainable Chem. Eng.* **8**, 17022–17032 (2020).
155. Luo, Y. et al. High thermoelectric performance in the new cubic semiconductor AgSnSbSe_3 by high entropy engineering. *J. Am. Chem. Soc.* **142**, 15187–15198 (2020).
156. Wang, X. et al. Enhanced thermoelectric performance in high entropy alloys $\text{Sn}_{0.25}\text{Pb}_{0.25}\text{Mn}_{0.25}\text{Ge}_{0.25}\text{Te}$. *ACS Appl. Mater. Interfaces* **13**, 18638–18647 (2021).
157. Cai, J. et al. Ultralow thermal conductivity and improved ZT of CuInTe_2 by high-entropy structure design. *Mater. Today Physics* **18**, 100394 (2021).
158. Zhang, R.-Z., Gucci, F., Zhu, H., Chen, K. & Reece, M. J. Data-driven design of ecofriendly thermoelectric high-entropy sulfides. *Inorg. Chem.* **57**, 13027–13033 (2018).

159. Jiang, B. et al. High figure-of-merit and power generation in high-entropy GeTe-based thermoelectrics. *Science* **377**, 208–213 (2022).
160. Jiang, B. et al. Entropy engineering promotes thermoelectric performance in p-type chalcogenides. *Nat. Commun.* **12**, 3234 (2021).
161. Huber, G. W., Iborra, S. & Corma, A. Synthesis of transportation fuels from biomass: chemistry, catalysts, and engineering. *Chem. Rev.* **106**, 4044–4098 (2006).
162. Sheldon, R. A. Green chemistry, catalysis and valorization of waste biomass. *J. Mol. Catal. a. Chem.* **422**, 3–12 (2016).
163. Fang, X., Kalathil, S. & Reisner, E. Semi-biological approaches to solar-to-chemical conversion. *Chem. Soc. Rev.* **49**, 4926–4952 (2020).
164. Zhou, C.-H., Xia, X., Lin, C.-X., Tong, D.-S. & Beltramini, J. Catalytic conversion of lignocellulosic biomass to fine chemicals and fuels. *Chem. Soc. Rev.* **40**, 5588–5617 (2011).
165. Qu, T., Guo, W., Shen, L., Xiao, J. & Zhao, K. Experimental study of biomass pyrolysis based on three major components: hemicellulose, cellulose, and lignin. *Ind. Eng. Chem. Res.* **50**, 10424–10433 (2011).
166. Wei, Y., Tong, X., Wang, J. & Guo, S. High entropy catalysts for synthesis of biofuels (C₇–C₁₇) via the adjustable carbon chain increasing of furfural (C₅) at mild temperature. *ACS Sustainable Chem. Eng.* **11**, 11353–11358 (2023).
167. Bhatia, S. K. et al. Recent developments in pretreatment technologies on lignocellulosic biomass: effect of key parameters, technological improvements, and challenges. *Bioresour. Technol.* **300**, 122724 (2020).
168. Zhang, C. & Wang, F. Catalytic lignin depolymerization to aromatic chemicals. *Acc. Chem. Res.* **53**, 470–484 (2020).
169. Sun, Y. et al. Selective hydrodeoxygenation of lignin-derived vanillin via hetero-structured high-entropy alloy/oxide catalysts. *Energy Environ. Mater.* **7**, e12638 (2024).
170. Ma, Y. et al. High-entropy energy materials: challenges and new opportunities. *Energy Environ. Sci.* **14**, 2883–2905 (2021).
171. Tong, C.-J. et al. Microstructure characterization of Al_xCoCrCuFeNi high-entropy alloy system with multiprincipal elements. *Metall. Mater. Trans. A* **36**, 881–893 (2005).
172. Hutz, A.-I., Pervolarakis, E., Remediakis, I. N., Kristoffersen, H. H. & Rossmeisl, J. Scaling relations on high-entropy alloy catalyst surfaces. *J. Phys. Chem. C* **128**, 10251–10258 (2024).
173. Chen, Z. W. et al. Machine-learning-driven high-entropy alloy catalyst discovery to circumvent the scaling relation for CO₂ reduction reaction. *ACS Catal.* **12**, 14864–14871 (2022).
174. Chen, L. et al. High-entropy alloy catalysts: high-throughput and machine learning-driven design. *J. Mater. Inform.* **2**, 10–20517 (2022).
175. Xu, T.-Y., Feng, H.-W., Liu, W., Wang, Y. & Zheng, H.-H. Opportunities and challenges of high-entropy materials in lithium-ion batteries. *Rare Met.* **43**, 4884–4902 (2024).
176. Strauss, F., Botros, M., Breitung, B. & Brezesinski, T. High-entropy and compositionally complex battery materials. *J. Appl. Phys.* **135**, 120901 (2024).
177. Ritter, T. G., Pappu, S. & Shahbazian-Yassar, R. Scalable synthesis methods for high-entropy nanoparticles. *Adv. Energy Sustain. Res.* **5**, 2300297 (2024).
178. Bolar, S., Ito, Y. & Fujita, T. Future prospects of high-entropy alloys as next-generation industrial electrode materials. *Chem. Sci.* **15**, 8664–8722 (2024).
179. Ritter, T. G., Pappu, S. & Shahbazian-Yassar, R. High-entropy materials for lithium batteries. *Batteries* **10**, 96 (2024).
180. Chen, J. et al. Stability and compressibility of cation-doped high-entropy oxide MgCoNiCuZnO₅. *J. Phys. Chem. C* **123**, 17735–17744 (2019).
181. Cao, Y. & Aspuru-Guzik, A. Accelerating discovery in organic redox flow batteries. *Nat. Comput. Sci.* **4**, 89–91 (2024).
182. Kotsonis, G. N., Rost, C. M., Harris, D. T. & Maria, J.-P. Epitaxial entropy-stabilized oxides: growth of chemically diverse phases via kinetic bombardment. *MRS Commun.* **8**, 1371–1377 (2018).
183. Hossain, M. D. et al. Carbon stoichiometry and mechanical properties of high entropy carbides. *Acta Mater.* **215**, 117051 (2021).
184. Dupuy, A. D., Kodera, Y. & Garay, J. E. Unprecedented electro-optic performance in lead-free transparent ceramics. *Adv. Mater.* **28**, 7970–7977 (2016).
185. Dupuy, A. D. et al. Hidden transformations in entropy-stabilized oxides. *J. Eur. Ceram. Soc.* **41**, 6660–6669 (2021).
186. Dupuy, A. D., Chellali, M. R., Hahn, H. & Schoenung, J. M. Nucleation and growth behavior of multicomponent secondary phases in entropy-stabilized oxides. *J. Mater. Res.* **38**, 198–214 (2022).
187. Dupuy, A. D. & Schoenung, J. M. Morphological evolution in nanostructured secondary phases in entropy stabilized oxides. *Mater. Charact.* **193**, 112301 (2022).
188. Vecchio, K. et al. Fermi energy engineering of enhanced plasticity in high-entropy carbides. *Acta Mater.* **276**, 120117 (2024).
189. Abe, J. O., Popoola, A. P. I., Ajenifuja, E. & Popoola, O. M. Hydrogen energy, economy and storage: review and recommendation. *Int. J. Hydrogen Energy* **44**, 15072–15086 (2019).
190. An, J., Han, M.-K. & Kim, S.-J. Synthesis of heavily Cu-doped Bi₂Te₃ nanoparticles and their thermoelectric properties. *J. Solid State Chem.* **270**, 407–412 (2019).
191. Anantharaj, S., Kannimuthu, K. & Kundu, S. Spinel cobalt titanium binary oxide as an all-non-precious water oxidation electrocatalyst in acid. *Inorg. Mater.* **58**, 8570–8576 (2019).
192. Androulakis, J. et al. Thermoelectrics from abundant chemical elements: high-performance nanostructured PbSe–PbS. *J. Am. Chem. Soc.* **133**, 10920–10927 (2011).
193. Bo, L. et al. Achieving high thermoelectric properties of Cu₂Se via lattice softening and phonon scattering mechanism. *ACS Appl. Energy Mater.* **5**, 6453–6461 (2022).
194. Bo, L. et al. Enhanced thermoelectric properties of Cu₃SbSe₄ via configurational entropy tuning. *J. Mater. Sci.* **57**, 4643–4651 (2022).
195. Butt, S. et al. Enhanced thermoelectricity in high-temperature beta-phase copper(I) selenides embedded with Cu₂Te nanoclusters. *ACS Appl. Mater. Interfaces* **8**, 15196–15204 (2016).
196. Butt, S. et al. One-step rapid synthesis of Cu₂Se with enhanced thermoelectric properties. *J. Alloys Compd.* **786**, 557–564 (2019).
197. Cai, Z.-X. et al. Nanoporous ultra-high-entropy alloys containing fourteen elements for water splitting electrocatalysis. *Chem. Sci.* **12**, 11306–11315 (2021).
198. Chang, S.-Q., Cheng, C.-C., Cheng, P.-Y., Huang, C.-L. & Lu, S.-Y. Pulse electrodeposited FeCoNiMnW high entropy alloys as efficient and stable bifunctional electrocatalysts for acidic water splitting. *Chem. Eng. J.* **446**, 137452 (2022).
199. Chen, L., Liu, Y., He, J., Tritt, T. M. & Poon, S. J. High thermoelectric figure of merit by resonant dopant in half-Heusler alloys. *AIP Adv.* **7** (2017).
200. Chen, S. et al. Mn-doped RuO₂ nanocrystals as highly active electrocatalysts for enhanced oxygen evolution in acidic media. *ACS Catal.* **10**, 1152–1160 (2019).
201. Chen, R. et al. Significantly optimized thermoelectric properties in high-symmetry cubic Cu₇PSe₆ compounds via entropy engineering. *J. Mater. Chem. A* **6**, 6493–6502 (2018).
202. Chen, K., Zhang, R., Bos, J.-W. G. & Reece, M. J. Synthesis and thermoelectric properties of high-entropy half-Heusler MFe_{1-x}Co_xSb (M = equimolar Ti, Zr, Hf, V, Nb, Ta). *J. Alloys Compd.* **892**, 162045 (2022).
203. Chen, Y.-X. et al. Understanding of the extremely low thermal conductivity in high-performance polycrystalline SnSe through potassium doping. *Adv. Func. Mater.* **26**, 6836–6845 (2016).
204. Chen, S. et al. Vacancy-based defect regulation for high thermoelectric performance in Ge₉Sb₂Te_{12-x} compounds. *ACS Appl. Mater. Interfaces* **12**, 19664–19673 (2020).

205. Cheng, B. et al. Solid-state hydrogen storage properties of Ti–V–Nb–Cr high-entropy alloys and the associated effects of transitional metals (M= Mn, Fe, Ni). *Acta Metall. Sin.-Engl.* **36**, 1113–1122 (2023).
206. Cherniushok, O. et al. Entropy-induced multivalley band structures improve thermoelectric performance in p-Cu₇P(S_xSe_{1-x})₆ argyrodites. *ACS Appl. Mater. Interfaces* **13**, 39606–39620 (2021).
207. Das, A., Acharyya, P., Das, S. & Biswas, K. High thermoelectric performance in entropy-driven Ge_{1-2x-y}Pb_xSn_xSb_yTe. *J. Mater. Chem. A* **11**, 12793–12801 (2023).
208. Deng, J. F. et al. Enhanced thermoelectric properties of (Pb_{1-x}Yb_xTe)_{0.15}(GeTe)_{0.85} composites due to phase separation and Yb doping. *J. Alloys Compd.* **585**, 173–177 (2014).
209. Dewangan, S. K., Sharma, V. K., Sahu, P. & Kumar, V. Synthesis and characterization of hydrogenated novel AlCrFeMnNiW high entropy alloy. *Int. J. Hydrogen Energy* **45**, 16984–16991 (2020).
210. Dong, Y., Li, H. & Xu, G. Thermoelectric performance of (GeTe)_{1-x}(Sb₂Te₃)_x fabricated by high pressure sintering method. *Mater. Res. Express* **6**, 1250h5 (2020).
211. Usman, M. R. Hydrogen storage methods: Review and current status. *Renew. Sustainable Energy Rev.* **167**, 112743 (2022).
212. Edalati, P. et al. Reversible room temperature hydrogen storage in high-entropy alloy TiZrCrMnFeNi. *Scr. Mater.* **178**, 387–390 (2020).
213. Fan, Z., Wang, H., Wu, Y., Liu, X. & Lu, Z. Thermoelectric performance of PbSnTeSe high-entropy alloys. *Mater. Res. Lett.* **5**, 187–194 (2017).
214. Fan, Z., Wang, H., Wu, Y., Liu, X. J. & Lu, Z. P. Thermoelectric high-entropy alloys with low lattice thermal conductivity. *RSC Adv.* **6**, 52164–52170 (2016).
215. Floriano, R. et al. Hydrogen storage in TiZrNbFeNi high entropy alloys, designed by thermodynamic calculations. *Int. J. Hydrogen Energy* **45**, 33759–33770 (2020).
216. Fu, C., Zhu, T., Liu, Y., Xie, H. & Zhao, X. Band engineering of high performance p-type FeNbSb based half-Heusler thermoelectric materials for figure of merit zT. *Energy Environ. Sci.* **8**, 216–220 (2015).
217. Fu, C. et al. Enhancing the figure of merit of heavy-band thermoelectric materials through hierarchical phonon scattering. *Adv. Sci.* **3** (2016).
218. Fu, C. et al. High band degeneracy contributes to high thermoelectric performance in p-type half-Heusler compounds. *Adv. Energy Mater.* **4**, 1400600 (2014).
219. Gałażka, K. et al. Improved thermoelectric performance of (Zr_{0.3}Hf_{0.7})NiSn half-Heusler compounds by Ta substitution. *J. Appl. Phys.* **115**, 183704 (2014).
220. Gao, R., Dai, Q., Du, F., Yan, D. & Dai, L. C₆₀-adsorbed single-walled carbon nanotubes as metal-free, pH-universal, and multifunctional catalysts for oxygen reduction, oxygen evolution, and hydrogen evolution. *J. Am. Chem. Soc.* **141**, 11658–11666 (2019).
221. Ge, R. et al. Ultrafine defective RuO₂ electrocatalyst integrated on carbon cloth for robust water oxidation in acidic media. *Adv. Energy Mater.* **9**, 1901313 (2019).
222. Guan, M. et al. Enhanced thermoelectric performance of quaternary Cu_{2-2x}Ag_{2x}Se_{1-x}S_x liquid-like chalcogenides. *ACS Appl. Mater. Interfaces* **11**, 13433–13440 (2019).
223. Hao, S. et al. Dopants fixation of Ruthenium for boosting acidic oxygen evolution stability and activity. *Nat. Commun.* **11**, 5368 (2020).
224. Hao, S. et al. Torsion strained iridium oxide for efficient acidic water oxidation in proton exchange membrane electrolyzers. *Nat. Nanotechnol.* **16**, 1371–1377 (2021).
225. He, W. et al. High thermoelectric performance in low-cost SnS_{0.91}Se_{0.09} crystals. *Science* **365**, 1418–1424 (2019).
226. Hu, L. et al. Entropy engineering of SnTe: multi-principal-element alloying leading to ultralow lattice thermal conductivity and state-of-the-art thermoelectric performance. *Adv. Energy Mater.* **8**, 1802116 (2018).
227. Hu, Q. et al. Remarkably high thermoelectric performance of Cu_{2-x}Li_xSe bulks with nanopores. *J. Mater. Chem. A* **6**, 23417–23424 (2018).
228. Huang, Z. et al. High thermoelectric performance of new rhombohedral phase of GeSe stabilized through alloying with AgSbSe₂. *Angew. Chem. Int. Ed.* **56**, 14113–14118 (2017).
229. Huang, Y. et al. Regulating the configurational entropy to improve the thermoelectric properties of (GeTe)_{1-x}(MnZnCdTe₃)_x alloys. *Materials* **15**, 6798 (2022).
230. Jiang, B. et al. Cu₆GeSe₆-based thermoelectric materials with an argyrodite structure. *J. Mater. Chem. C* **5**, 943–952 (2017).
231. Jiang, B. et al. Entropy optimized phase transitions and improved thermoelectric performance in n-type liquid-like Ag₉GaSe₆ materials. *Mater. Today Physics* **5**, 20–28 (2018).
232. Jiang, B. et al. Mesoporous metallic iridium nanosheets. *J. Am. Chem. Soc.* **140**, 12434–12441 (2018).
233. Jin, Z. et al. Nanoporous Al-Ni-Co-Ir-Mo high-entropy alloy for record-high water splitting activity in acidic environments. *Small* **15**, 1904180 (2019).
234. Jo, S. et al. Nonprecious high-entropy chalcogenide glasses-based electrocatalysts for efficient and stable acidic oxygen evolution reaction in proton exchange membrane water electrolysis. *Adv. Energy Mater.* **13**, 2301420 (2023).
235. Kato, K. et al. Flexible porous bismuth telluride thin films with enhanced figure of merit using micro-phase separation of block copolymer. *Adv. Mater. Interfaces* **1**, 1300015 (2014).
236. Khan, T. T., Kim, I.-H. & Ur, S.-C. Improvement of the thermoelectric properties of the perovskite SrTiO₃ by Cr-doping. *J. Elec. Mater.* **48**, 1864–1869 (2019).
237. Kim, S. I. et al. Dense dislocation arrays embedded in grain boundaries for high-performance bulk thermoelectrics. *Science* **348**, 109–114 (2015).
238. Kim, M. J. et al. Effects of Cl-doping on thermoelectric transport properties of Cu₂Se prepared by spark plasma sintering. *J. Elec. Mater.* **48**, 1958–1964 (2019).
239. Kunce, I., Polański, M. & Czujko, T. Microstructures and hydrogen storage properties of La-Ni-Fe-V-Mn alloys. *Int. J. Hydrogen Energy* **42**, 27154–27164 (2017).
240. Kunce, I., Polański, M. & Bystrzycki, J. Structure and hydrogen storage properties of a high entropy ZrTiVCrFeNi alloy synthesized using Laser Engineered Net Shaping (LENS). *Int. J. Hydrogen Energy* **38**, 12180–12189 (2013).
241. Kwong, W. L., Lee, C. C., Shchukarev, A. & Messinger, J. Cobalt-doped hematite thin films for electrocatalytic water oxidation in highly acidic media. *Chem. Comm.* **55**, 5017–5020 (2019).
242. Kwong, W. L., Lee, C. C., Shchukarev, A., Björn, E. & Messinger, J. High-performance iron (III) oxide electrocatalyst for water oxidation in strongly acidic media. *J. Catal.* **365**, 29–35 (2018).
243. Lai, Q., Vedyappan, V., Aguey-Zinsou, K.-F. & Matsumoto, H. One-step synthesis of carbon-protected Co₃O₄ nanoparticles toward long-term water oxidation in acidic media. *Adv. Energy Sustain. Res.* **2**, 2100086 (2021).
244. Lan, J.-L. et al. Enhanced thermoelectric properties of Pb-doped BiCuSeO ceramics. *Adv. Mater.* **25**, 5086–5090 (2013).
245. Lee, S. et al. Thermoelectric properties of n-type half-Heusler compounds synthesized by the induction melting method. *Trans. Electr. Electron. Mater.* **16**, 342–345 (2015).
246. Lei, Y. et al. Microwave synthesis, microstructure, and thermoelectric properties of Zr substituted Zr_xTi_{1-x}NiSn half-Heusler bulks. *Mater. Lett.* **201**, 189–193 (2017).
247. Lettermeier, P. et al. Nanosized IrO_x–Ir catalyst with relevant activity for anodes of proton exchange membrane electrolysis produced by a cost-effective procedure. *Angew. Chem. Int. Ed.* **55**, 742–746 (2016).

248. Li, G. et al. Boosted performance of Ir species by employing TiN as the support toward oxygen evolution reaction. *ACS Appl. Mater. Interfaces* **10**, 38117–38124 (2018).
249. Li, S. et al. Heavy doping by bromine to improve the thermoelectric properties of n-type polycrystalline SnSe. *Adv. Sci.* **5**, 1800598 (2018).
250. Li, R. et al. IrW nanochannel support enabling ultrastable electrocatalytic oxygen evolution at 2 A cm⁻² in acidic media. *Nat. Commun.* **12**, 3540 (2021).
251. Liang, G. et al. (GeTe)_{1-x}(AgSnSe₂)_x: Strong atomic disorder-induced high thermoelectric performance near the Ioffe-Regel limit. *ACS Appl. Mater. Interfaces* **13**, 47081–47089 (2021).
252. Lin, X. et al. Inhibited surface diffusion of high-entropy nano-alloys for the preparation of 3D nanoporous graphene with high amounts of single atom dopants. *ACS Mater. Lett.* **4**, 978–986 (2022).
253. Liu, K.-J. et al. Entropy engineering in CaZn₂Sb₂-YbMg₂Sb₂ Zintl alloys for enhanced thermoelectric performance. *Rare Met.* **41**, 2998–3004 (2022).
254. Liu, Z. et al. Phase-transition temperature suppression to achieve cubic GeTe and high thermoelectric performance by Bi and Mn codoping. *Proc. Natl. Acad. Sci.* **115**, 5332–5337 (2018).
255. Liu, H., Peng, X., Liu, X., Qi, G. & Luo, J. Porous Mn-doped FeP/Co₃(PO₄)₂ nanosheets as efficient electrocatalysts for overall water splitting in a wide pH range. *ChemSusChem* **12**, 1334–1341 (2019).
256. Liu, X. et al. Restructuring highly electron-deficient metal-metal oxides for boosting stability in acidic oxygen evolution reaction. *Nat. Commun.* **12**, 5676 (2021).
257. Luo, P., Mao, Y., Li, Z., Zhang, J. & Luo, J. Entropy engineering: a simple route to both p- and n-type thermoelectrics from the same parent material. *Mater. Today Physics* **26**, 100745 (2022).
258. Luo, L. et al. Nanoscale microstructure and hydrogen storage performance of as-cast La-containing V-based multicomponent alloys. *Int. J. Hydrogen Energy* **47**, 34165–34182 (2022).
259. Luo, Z.-Z. et al. Soft phonon modes from off-center Ge atoms lead to ultralow thermal conductivity and superior thermoelectric performance in n-type PbSe–GeSe. *Energy Environ. Sci.* **11**, 3220–3230 (2018).
260. Ma, Z. et al. High thermoelectric performance and low lattice thermal conductivity in lattice-distorted high-entropy semiconductors AgMnSn_{1-x}Pb_xSbTe₄. *Chem. Mater.* **34**, 8959–8967 (2022).
261. Miao, X. et al. Quadruple perovskite ruthenate as a highly efficient catalyst for acidic water oxidation. *Nat. Commun.* **10**, 3809 (2019).
262. Mondschein, J. S. et al. Crystalline cobalt oxide films for sustained electrocatalytic oxygen evolution under strongly acidic conditions. *Chem. Mater.* **29**, 950–957 (2017).
263. Montero, J. et al. How 10 at changes hydrogen sorption properties. *Molecules* **26**, 2470 (2021).
264. Montero, J. et al. Hydrogen storage properties of the refractory Ti-V-Zr-Nb-Ta multi-principal element alloy. *J. Alloys Compd.* **835**, 155376 (2020).
265. Montero, J., Ek, G., Sahlberg, M. & Zlotea, C. Improving the hydrogen cycling properties by Mg addition in Ti-V-Zr-Nb refractory high entropy alloy. *Scr. Mater.* **194**, 113699 (2021).
266. Montero, J. et al. TiVZrNb multi-principal-element alloy: synthesis optimization, structural and hydrogen sorption properties. *Molecules* **24**, 2799 (2019).
267. Munir, A. et al. Controlled engineering of nickel carbide induced N-enriched carbon nanotubes for hydrogen and oxygen evolution reactions in wide pH range. *Electrochim. Acta* **341**, 136032 (2020).
268. Nshimiyimana, E. et al. Discordant nature of Cd in GeTe enhances phonon scattering and improves band convergence for high thermoelectric performance. *J. Mater. Chem. A* **8**, 1193–1204 (2020).
269. Nshimiyimana, E. et al. Realization of non-equilibrium process for high thermoelectric performance Sb-doped GeTe. *Sci. Bull.* **63**, 717–725 (2018).
270. Nygård, M. M. et al. Counting electrons – a new approach to tailor the hydrogen sorption properties of high-entropy alloys. *Acta Mater.* **175**, 121–129 (2019).
271. Park, K. et al. Colloidal synthesis and thermoelectric properties of La-doped SrTiO₃ nanoparticles. *J. Mater. Chem. A* **2**, 4217–4224 (2014).
272. Qiu, X. et al. Effect of Bi doping on thermoelectric properties of Ge_{0.90-x}Pb_{0.10}B_xTe compounds. *Mat. Sci. Semicond. Proc.* **109**, 104955 (2020).
273. Raja, D. S. et al. In-situ grown metal-organic framework-derived carbon-coated Fe-doped cobalt oxide nanocomposite on fluorine-doped tin oxide glass for acidic oxygen evolution reaction. *Appl. Catal. B* **303**, 120899 (2022).
274. Raphel, A., Vivekanandhan, P. & Kumaran, S. High entropy phenomena induced low thermal conductivity in BiSbTe_{1.5}Se_{1.5} thermoelectric alloy through mechanical alloying and spark plasma sintering. *Mater. Lett.* **269**, 127672 (2020).
275. Rausch, E., Balke, B., Ouardi, S. & Felser, C. Enhanced thermoelectric performance in the p-type half-Heusler (Ti/Zr/Hf) CoSb_{0.8}Sn_{0.2} system via phase separation. *Phys. Chem. Chem. Phys.* **16**, 25258–25262 (2014).
276. Ren, X. et al. An efficient electrocatalyst based on vertically aligned heteroatom (B/N/P/O/S)-doped graphene array integrated with FeCoNiP nanoparticles for overall water splitting. *Adv. Sustainable Syst.* **6**, 2100436 (2022).
277. Ren, G. et al. Electrical and thermal transport behavior in Zn-doped BiCuSeO oxyselenides. *J. Elec. Mater.* **44**, 1627–1631 (2015).
278. Samanta, M., Ghosh, T., Arora, R., Waghmare, U. V. & Biswas, K. Realization of both n- and p-type GeTe thermoelectrics: electronic structure modulation by AgBiSe₂ alloying. *J. Am. Chem. Soc.* **141**, 19505–19512 (2019).
279. Samanta, M., Roychowdhury, S., Ghatak, J., Perumal, S. & Biswas, K. Ultrahigh average thermoelectric figure of merit, low lattice thermal conductivity and enhanced microhardness in nanostructured (GeTe)_x(AgSbSe₂)_{100-x}. *Chem. Eur. J.* **23**, 7438–7443 (2017).
280. Schlapbach, L. & Züttel, A. Hydrogen-storage materials for mobile applications. *Nature* **414**, 353–358 (2001).
281. Shen, H. et al. Compositional dependence of hydrogenation performance of Ti-Zr-Hf-Mo-Nb high entropy alloys for hydrogen/tritium storage. *J. Mater. Sci. Technol.* **55**, 116–125 (2020).
282. Shen, H. et al. A novel TiZrHfMoNb high entropy alloys for solar thermal energy storage. *Nanomater.* **9**, 248 (2019).
283. Shi, W. et al. Preparation and thermoelectric properties of yttrium-doped Bi₂Te₃ flower-like nanopowders. *J. Elec. Mater.* **43**, 3162–3168 (2014).
284. Shuai, J. et al. Higher thermoelectric performance of Zintl phases (Eu_{0.5}Yb_{0.5})_{1-x}Ca_xMg₂Bi₂ by band engineering and strain fluctuation. *Proc. Natl. Acad. Sci.* **113**, E4125–E4132 (2016).
285. Silva, B. H., Zlotea, C., Champion, Y., Botta, W. J. & Zepton, G. Design of TiVNb-(Cr, Ni or Co) multicomponent alloys with the same valence electron concentration for hydrogen storage. *J. Alloys Compd.* **865**, 158767 (2021).
286. Singh, N. K., Pandey, J., Acharya, S. & Soni, A. Charge carriers modulation and thermoelectric performance of intrinsically p-type Bi₂Te₃ by Ge doping. *J. Alloys Compd.* **746**, 350–355 (2018).
287. Sleiman, S. & Huot, J. Effect of particle size, pressure and temperature on the activation process of hydrogen absorption in TiVZrHfNb high entropy alloy. *J. Alloys Compd.* **861**, 158615 (2021).
288. Strozi, R. B., Leiva, D. R., Huot, J., Botta, W. J. & Zepton, G. Synthesis and hydrogen storage behavior of Mg-V-Al-Cr-Ni high entropy alloys. *Int. J. Hydrogen Energy* **46**, 2351–2361 (2021).

289. Su, J. et al. Assembling ultrasmall copper-doped ruthenium oxide nanocrystals into hollow porous polyhedra: highly robust electrocatalysts for oxygen evolution in acidic media. *Adv. Mater.* **30**, 1801351 (2018).
290. Su, H. et al. In-situ spectroscopic observation of dynamic-coupling oxygen on atomically dispersed iridium electrocatalyst for acidic water oxidation. *Nat. Commun.* **12**, 6118 (2021).
291. Suwardi, A. et al. Tailoring the phase transition temperature to achieve high-performance cubic GeTe-based thermoelectrics. *J. Mater. Chem. A* **8**, 18880–18890 (2020).
292. Tackett, B. M. et al. Reducing iridium loading in oxygen evolution reaction electrocatalysts using core–shell particles with nitride cores. *ACS Catal.* **8**, 2615–2621 (2018).
293. Tajuddin, A. A. H. et al. Corrosion-resistant and high-entropic non-noble-metal electrodes for oxygen evolution in acidic media. *Adv. Mater.* **35**, 2207466 (2023).
294. Tan, H. et al. Rapid preparation of $\text{Ge}_{0.9}\text{Sb}_{0.1}\text{Te}_{1+x}$ via unique melt spinning: Hierarchical microstructure and improved thermoelectric performance. *J. Alloys Compd.* **774**, 129–136 (2019).
295. Tang, G. et al. Realizing high thermoelectric performance below phase transition temperature in polycrystalline SnSe via lattice anharmonicity strengthening and strain engineering. *ACS Appl. Mater. Interfaces* **10**, 30558–30565 (2018).
296. Tian, Y. et al. A Co-doped nanorod-like RuO_2 electrocatalyst with abundant oxygen vacancies for acidic water oxidation. *Iscience* **23** (2020).
297. Nguyen, D. V. et al. Synthesis and thermoelectric properties of Ti-substituted $(\text{Hf}_{0.5}\text{Zr}_{0.5})(1-x)\text{Ti}_x\text{NiSn}_{0.998}\text{Sb}_{0.002}$ half-Heusler compounds. *J. Alloys Compd.* **773**, 1141–1145 (2019).
298. Wang, Y. & Wang, Y. Recent advances in additive-enhanced magnesium hydride for hydrogen storage. *Prog. Nat. Sci.-Mater.* **27**, 41–49 (2017).
299. Wang, X.-Y. et al. Attaining reduced lattice thermal conductivity and enhanced electrical conductivity in as-sintered pure n-type Bi_2Te_3 alloy. *J. Mater. Sci.* **54**, 4788–4797 (2019).
300. Wang, X. et al. Band modulation and strain fluctuation for realizing high average zT in GeTe. *Adv. Energy Mater.* **12**, 2201043 (2022).
301. Wang, J., Liu, B., Miao, N., Zhou, J. & Sun, Z. I-doped Cu_2Se nanocrystals for high-performance thermoelectric applications. *J. Alloys Compd.* **772**, 366–370 (2019).
302. Wang, X. et al. Orbital alignment for high performance thermoelectric YbCd_2Sb_2 alloys. *Chem. Mater.* **30**, 5339–5345 (2018).
303. Wang, H., Pei, Y., LaLonde, A. D. & Snyder, G. J. Weak electron–phonon coupling contributing to high thermoelectric performance in n-type PbSe. *Proc. Natl. Acad. Sci.* **109**, 9705–9709 (2012).
304. Wei, W. et al. Achieving high thermoelectric figure of merit in polycrystalline SnSe via introducing Sn vacancies. *J. Am. Chem. Soc.* **140**, 499–505 (2018).
305. Wu, J. et al. Exfoliated 2D transition metal disulfides for enhanced electrocatalysis of oxygen evolution reaction in acidic medium. *Adv. Mater. Interfaces* **3**, 1500669 (2016).
306. Xia, K. et al. Enhanced thermoelectric performance in 18-electron $\text{Nb}_{0.8}\text{CoSb}$ half-Heusler compound with intrinsic Nb vacancies. *Adv. Func. Mater.* **28**, 1705845 (2018).
307. Xie, L. et al. Stacking faults modulation for scattering optimization in GeTe-based thermoelectric materials. *Nano Energy* **68**, 104347 (2020).
308. Xing, T. et al. Superior performance and high service stability for GeTe-based thermoelectric compounds. *Natl. Sci. Rev.* **6**, 944–954 (2019).
309. Xiong, Q. et al. One-step synthesis of cobalt-doped MoS_2 nanosheets as bifunctional electrocatalysts for overall water splitting under both acidic and alkaline conditions. *Chem. Comm.* **54**, 3859–3862 (2018).
310. Xu, J. et al. Strong electronic coupling between ultrafine iridium–ruthenium nanoclusters and conductive, acid-stable tellurium nanoparticle support for efficient and durable oxygen evolution in acidic and neutral media. *ACS Catal.* **10**, 3571–3579 (2020).
311. Yan, K.-L. et al. Probing the active sites of Co_3O_4 for the acidic oxygen evolution reaction by modulating the $\text{Co}^{2+}/\text{Co}^{3+}$ ratio. *J. Mater. Chem. A* **6**, 5678–5686 (2018).
312. Yang, X. et al. Highly acid-durable carbon coated Co_3O_4 nanoarrays as efficient oxygen evolution electrocatalysts. *Nano Energy* **25**, 42–50 (2016).
313. Yang, C. et al. Ultralow thermal conductivity and enhanced thermoelectric properties in a textured $(\text{Ca}_{0.35}\text{Sr}_{0.2}\text{Ba}_{0.15}\text{Na}_{0.2}\text{Bi}_{0.1})_3\text{Co}_4\text{O}_9$ high-entropy ceramic. *J. Alloys Compd.* **940**, 168802 (2023).
314. Yao, J. et al. Stable cubic crystal structures and optimized thermoelectric performance of SrTiO_3 -based ceramics driven by entropy engineering. *J. Mater. Chem. A* **10**, 24561–24572 (2022).
315. Yao, L. et al. Sub-2 nm IrRuNiMoCo high-entropy alloy with iridium-rich medium-entropy oxide shell to boost acidic oxygen evolution. *Adv. Mater.* **36**, 2314049 (2024).
316. Yu, J. et al. Unique role of refractory Ta alloying in enhancing the figure of merit of NbFeSb thermoelectric materials. *Adv. Energy Mater.* **8**, 1701313 (2018).
317. Yue, L. et al. Cu/Sb codoping for tuning carrier concentration and thermoelectric performance of GeTe-based alloys with ultralow lattice thermal conductivity. *ACS Appl. Energy Mater.* **2**, 2596–2603 (2019).
318. Zaluska, A., Zaluski, L. & Ström-Olsen, J. O. Nanocrystalline magnesium for hydrogen storage. *J. Alloys Compd.* **288**, 217–225 (1999).
319. Zepton, G. et al. Hydrogen induced phase transition of $\text{MgZrTiFe}_{0.5}\text{Co}_{0.5}\text{Ni}_{0.5}$ high entropy alloy. *Int. J. Hydrogen Energy* **43**, 1702–1708 (2018).
320. Zhang, Z. et al. A dual role by incorporation of magnesium in YbZn_2Sb_2 Zintl phase for enhanced thermoelectric performance. *Adv. Energy Mater.* **10**, 2001229 (2020).
321. Zhang, C. et al. Enhanced thermoelectric performance of solution-derived bismuth telluride based nanocomposites via liquid-phase sintering. *Nano Energy* **30**, 630–638 (2016).
322. Zhang, Z. et al. Entropy engineering induced exceptional thermoelectric and mechanical performances in $\text{Cu}_{2-y}\text{Ag}_y\text{Te}_{1-2x}\text{S}_x\text{Se}_x$. *Acta Mater.* **224**, 117512 (2022).
323. Zhang, P. et al. High-entropy $(\text{Ca}_{0.2}\text{Sr}_{0.2}\text{Ba}_{0.2}\text{La}_{0.2}\text{Pb}_{0.2})\text{TiO}_3$ perovskite ceramics with A-site short-range disorder for thermoelectric applications. *J. Mater. Sci. Technol.* **97**, 182–189 (2022).
324. Zhang, D. et al. High-entropy alloy metallene for highly efficient overall water splitting in acidic media. *Chin. J. Cat.* **45**, 174–183 (2023).
325. Zhang, Q. et al. High-performance thermoelectric material and module driven by medium-entropy engineering in SnTe. *Adv. Func. Mater.* **32**, 2205458 (2022).
326. Zhang, D.-B., Li, H.-Z., Zhang, B.-P., Liang, D.-D. & Xia, M. Hybrid-structured ZnO thermoelectric materials with high carrier mobility and reduced thermal conductivity. *RSC Adv.* **7**, 10855–10864 (2017).
327. Zhang, Q. et al. Raised solubility in SnTe by GeMnTe_2 alloying enables converged valence bands, low thermal conductivity, and high thermoelectric performance. *Nano Energy* **94**, 106940 (2022).
328. Zhang, P. et al. Reduced lattice thermal conductivity of perovskite-type high-entropy $(\text{Ca}_{0.25}\text{Sr}_{0.25}\text{Ba}_{0.25}\text{RE}_{0.25})\text{TiO}_3$ ceramics by phonon engineering for thermoelectric applications. *J. Alloys Compd.* **898**, 162858 (2022).

329. Zhang, H. et al. Synthesis and thermoelectric properties of n-type half-Heusler compound VCoSb with valence electron count of 19. *J. Alloys Compd.* **654**, 321–326 (2016).
330. Zhang, X. et al. Ultralow lattice thermal conductivity and improved thermoelectric performance in a Hf-free half-Heusler compound modulated by entropy engineering. *J. Mater. Chem. A* **11**, 8150–8161 (2023).
331. Zhao, K. et al. High thermoelectric performance and low thermal conductivity in $\text{Cu}_{2-y}\text{S}_{1/3}\text{Se}_{1/3}\text{Te}_{1/3}$ liquid-like materials with nanoscale mosaic structures. *Nano Energy* **42**, 43–50 (2017).
332. Zhao, D., Wang, L., Bo, L. & Wu, D. Synthesis and thermoelectric properties of Ni-doped ZrCoSb half-Heusler compounds. *Metals* **8**, 61 (2018).
333. Zhao, K. et al. Thermoelectric materials with crystal-amorphicity duality induced by large atomic size mismatch. *Joule* **5**, 1183–1195 (2021).
334. Zheng, Z. et al. Rhombohedral to cubic conversion of GeTe via MnTe alloying leads to ultralow thermal conductivity, electronic band convergence, and high thermoelectric performance. *J. Am. Chem. Soc.* **140**, 2673–2686 (2018).
335. Zhong, J. et al. Entropy engineering enhances the thermoelectric performance and microhardness of $(\text{GeTe})_{1-x}(\text{AgSb}_{0.5}\text{Bi}_{0.5}\text{Te}_2)_x$. *Sci. China Mater.* **66**, 696–706 (2023).
336. Zhong, B. et al. High superionic conduction arising from aligned large lamellae and large figure of merit in bulk $\text{Cu}_{1.94}\text{Al}_{0.02}\text{Se}$. *Appl. Phys. Lett.* **105**, 123902 (2014).
337. Zhu, H. et al. Discovery of TaFeSb-based half-Heuslers with high thermoelectric performance. *Nat. Commun.* **10**, 270 (2019).
338. Zhu, H. et al. Discovery of ZrCoBi-based half Heuslers with high thermoelectric conversion efficiency. *Nat. Commun.* **9**, 2497 (2018).
339. Zhu, Z., Zhang, Y., Song, H. & Li, X.-J. Enhancement of thermoelectric performance of $\text{Cu}_{1.98}\text{Se}$ by Pb doping. *Appl. Phys. A* **124**, 1–7 (2018).
340. Zhu, Z., Zhang, Y., Song, H. & Li, X.-J. Enhancement of thermoelectric performance of Cu_2Se by K doping. *Appl. Phys. A* **124**, 871 (2018).
341. O. de Marco, M., Li, Y., Li, H.-W., Edalati, K. & Floriano, R. Mechanical synthesis and hydrogen storage characterization of MgVCr and MgVTiCrFe high entropy alloy. *Adv. Energy Mater.* **22**, 1901079 (2020).
342. Yan, X. et al. Stronger phonon scattering by larger differences in atomic mass and size in p-type half-Heuslers $\text{Hf}_{1-x}\text{Ti}_x\text{CoSb}_{0.8}\text{Sn}_{0.2}$. *Energy Environ. Sci.* **5**, 7543–7548 (2012).
343. Kusne, A. G. et al. On-the-fly closed-loop materials discovery via Bayesian active learning. *Nat. Commun.* **11**, 5966 (2020).
344. Kumar, A. et al. Solid-state reaction synthesis of nanoscale materials: strategies and applications. *Chem. Rev.* **122**, 12748–12863 (2022).
345. Parkinson, B. The emerging art of solid-state synthesis. *Science* **270**, 1157–1158 (1995).
346. Cavaliere, P., Sadeghi, B. & Shabani, A. *Spark Plasma Sintering: Process Fundamentals* (Springer International Publishing, 2019) 3–20.
347. Nadagouda, M. N., Speth, T. F. & Varma, R. S. Microwave-assisted green synthesis of silver nanostructures. *Acc. Chem. Res.* **44**, 469–478 (2011).
348. Demazeau, G. High pressure in solid-state chemistry. *J. Phys.: Condens. Matter* **14**, 11031 (2002).
349. Mori, K., Shimada, Y., Yoshida, H., Hinuma, Y. & Yamashita, H. Entropy-stabilized isolated active Pd species within a high-entropy fluorite oxide matrix for CO_2 hydrogenation to formic acid. *ACS Appl. Nano Mater.* **7**, 28649–28658 (2024).
350. Araujo, R. B. & Edvinsson, T. Supervised AI and deep neural networks to evaluate high-entropy alloys as reduction catalysts in aqueous environments. *ACS Catal.* **14**, 3742–3755 (2024).
351. Rittirum, M. et al. First-principles density functional theory and machine learning technique for the prediction of water adsorption site on PtPd-based high-entropy-alloy catalysts. *Adv. Theory Simul.* **6**, 2200926 (2023).
352. Oh, S.-H. V., Yoo, S.-H. & Jang, W. Small dataset machine-learning approach for efficient design space exploration: engineering ZnTe-based high-entropy alloys for water splitting. *npj Comput. Mater.* **10**, 166 (2024).
353. Mehrabi-Kalajahi, S. et al. $(\text{CoFeMnCuNiCr})_3\text{O}_4$ high-entropy oxide nanoparticles immobilized on reduced graphene oxide as heterogeneous catalysts for solvent-free aerobic oxidation of benzyl alcohol. *ACS Appl. Nano Mater.* **7**, 5513–5524 (2024).
354. Plenge, M. K., Pedersen, J. K., Mints, V. A., Arenz, M. & Rossmeisl, J. Following paths of maximum catalytic activity in the composition space of high-entropy alloys. *Adv. Energy Mater.* **13**, 2202962 (2023).
355. Ludwig, A. Discovery of new materials using combinatorial synthesis and high-throughput characterization of thin-film materials libraries combined with computational methods. *npj Comput. Mater.* **5**, 70 (2019).
356. Sun, C., Goel, R. & Kulkarni, A. R. Developing cheap but useful machine learning-based models for investigating high-entropy alloy catalysts. *Langmuir* **40**, 3691–3701 (2024).
357. Tamtaji, M., Kazemeini, M. & Abdi, J. DFT and machine learning studies on a multi-functional single-atom catalyst for enhanced oxygen and hydrogen evolution as well as CO_2 reduction reactions. *Int. J. Hydrogen Energy* **80**, 1075–1083 (2024).
358. He, X. Correlating nitrate adsorption with the local environments of FeCoNiCuZn high-entropy alloy catalysts using machine learning. *Langmuir* **40**, 15503–15511 (2024).
359. Chen, L. et al. Giant energy-storage density with ultrahigh efficiency in lead-free relaxors via high-entropy design. *Nature* **13**, 3089 (2022).
360. Yang, B. et al. High-entropy enhanced capacitive energy storage. *Nat. Mater.* **21**, 1074–1080 (2022).
361. Song, M. et al. Electrical conductivities and conduction mechanism of lithium-doped high-entropy oxides at different temperature and pressure conditions. *JACS Au* **4**, 592–606 (2024).
362. Wang, D., Liu, L., Huang, W. & Zhuang, H. L. Semiconducting SiGeSn high-entropy alloy: a density functional theory study. *J. Appl. Phys.* **126**, 225703 (2019).
363. Wang, D., Xu, Y., Zhang, H. & Zhang, Y. An $A_2B_2O_7$ -type high-entropy oxide for efficient photoelectrochemical photodetector with excellent long-term stability. *Small Methods* **8**, 2300888 (2024).
364. Edalati, P. et al. High-entropy oxynitride as a low-bandgap and stable photocatalyst for hydrogen production. *J. Mater. Chem. A* **9**, 15076–15086 (2021).
365. Usharani, N. J., Arivazhagan, P., Thomas, T. & Bhattacharya, S. S. Factors determining the band gap of a nanocrystalline multicomponent equimolar transition metal based high entropy oxide $(\text{Co,Cu,Mg,Ni,Zn})\text{O}$. *Mater. Sci. Eng. B* **283**, 115847 (2022).
366. Chang, S. C., Chen, H.-Y., Chen, P.-H., Lee, J.-T. & Wu, J. M. Piezo-photocatalysts based on a ferroelectric high-entropy oxide. *Appl. Catal. B* **324**, 122204 (2023).
367. Ma, Z. et al. High entropy semiconductor AgMnGeSbTe_4 with desirable thermoelectric performance. *Adv. Func. Mater.* **31**, 2103197 (2021).
368. Lou, Z. et al. A novel high-entropy perovskite ceramics $\text{Sr}_{0.9}\text{La}_{0.1}(\text{Zr}_{0.25}\text{Sn}_{0.25}\text{Ti}_{0.25}\text{Hf}_{0.25})\text{O}_3$ with low thermal conductivity and high Seebeck coefficient. *J. Eur. Ceram. Soc.* **42**, 3480–3488 (2022).
369. Lei, B., Li, G.-R., Chen, P. & Gao, X.-P. A solar rechargeable battery based on hydrogen storage mechanism in dual-phase electrolyte. *Nano Energy* **38**, 257–262 (2017).
370. Pedersen, J. K., Batchelor, T. A. A., Bagger, A. & Rossmeisl, J. High-entropy alloys as catalysts for the CO_2 and CO reduction reactions. *ACS Catal.* **10**, 2169–2176 (2020).
371. Wang, Q. et al. High entropy liquid electrolytes for lithium batteries. *Nat. Commun.* **14**, 440 (2023).

Acknowledgements

The authors thank Matthew Brownrigg, Gabrielle Ameyaw, Akshaya Ajith, Shawn Zhou, Katrina Wang, and Jaehyung Lee for helpful discussions. Research was sponsored by the Advanced Research Projects Agency-Energy (ARPA-E) (DE-AR0001787). G.Q. acknowledges support from the Ralph O'Connor Sustainable Energy Institute (ROSEI) at JHU. X.X. acknowledges support from the Institute for Data-Intensive Engineering and Science (IDIES) at JHU. K.C. acknowledges support from the Maryland Space Grant Consortium (MDSGC) and the Space@Hopkins seed grant fund. C.O. acknowledges support from Advanced Research Computing at Hopkins (ARCH).

Author contributions

C.O. conceived and initialized the study. C.O. and G.Q. developed the manuscript outline and led the collaboration. G.Q., T.L., X.X., Y.L., and C.O. performed the literature review. All authors (G.Q., T.L., X.X., Y.L., M.N., K.C., and C.O.) contributed to the writing of the manuscript.

Competing interests

The authors declare no competing interests.

Additional information

Supplementary information The online version contains supplementary material available at

<https://doi.org/10.1038/s41524-025-01594-6>.

Correspondence and requests for materials should be addressed to Corey Oses.

Reprints and permissions information is available at <http://www.nature.com/reprints>

Publisher's note Springer Nature remains neutral with regard to jurisdictional claims in published maps and institutional affiliations.

Open Access This article is licensed under a Creative Commons Attribution-NonCommercial-NoDerivatives 4.0 International License, which permits any non-commercial use, sharing, distribution and reproduction in any medium or format, as long as you give appropriate credit to the original author(s) and the source, provide a link to the Creative Commons licence, and indicate if you modified the licensed material. You do not have permission under this licence to share adapted material derived from this article or parts of it. The images or other third party material in this article are included in the article's Creative Commons licence, unless indicated otherwise in a credit line to the material. If material is not included in the article's Creative Commons licence and your intended use is not permitted by statutory regulation or exceeds the permitted use, you will need to obtain permission directly from the copyright holder. To view a copy of this licence, visit <http://creativecommons.org/licenses/by-nc-nd/4.0/>.

© The Author(s) 2025